A comprehensive and practical framework for advanced battery management system of vanadium redox flow batteries

Hao Wang^{a,*}, S. Ali Pourmousavi^a, Wen L. Soong^a, Xinan Zhang^b, Aleksandar N. Nikoloski^c, Nesimi Ertugrul^a

^a School of Electrical & Mechanical Engineering, The University of Adelaide, Australia ^b School of Engineering, The University of Western Australia, Australia ^c Harry Butler Institute (Centre for Water Energy and Waste), College of Science, Health, Engineering and Education, Murdoch University, Australia

Abstract

27

The practical and effective design of the battery management system (BMS) is crucial to achieving high performance, long service life, and safe operation of all battery types, including vanadium redox flow batteries (VRFBs). However, without having a comprehensive and practical battery management scheme design as the foundation to develop an industrial or commercialscale BMS for VRFBs, various underlying factors that promote the deployment of VRFBs in many projects that incorporate renewable energy sources (RESs) for decarbonisation resulting in economic benefits cannot be accomplished. In this paper, an advanced VRFB-BMS scheme is proposed that achieves high performance in state of charge (SOC) estimation, hydraulic control and thermal management without requiring excessive computational resources. Rigorous validations of this proposed VRFB-BMS scheme are carried out based on a state-of-the-art zerodimensional (0-D) model to demonstrate the performance of the proposed BMS scheme design including case studies that showed: (1) a 8.1% increase in round-trip efficiency; (2) automatic capacity rebalancing and highly accurate half-system SOC estimation method with a mean absolute percentage error (MAPE) less than 1% when the system is severely imbalanced; and (3) the ability to conduct effective thermal management with the use of a heating, ventilation and air-conditioning system (HVAC). The studies also demonstrated the capability of integrating the BMS with the energy management system (EMS) to achieve specified objectives for the users. This can bring numerous economic and environmental benefits to satisfy the objectives of the decision-makers or the investors.

²⁹ Keywords: Vanadium redox flow battery; Battery modelling; Battery management system;

Energy management system; Thermal management

 ${\it Email~address:}~hao.wang 05@adelaide.edu.au$

^{*}Corresponding Author

Nomenclature

Home energy management system

3 α_{ch}, β_{ch} Charge power regulation coefficients

4 α_{dch} , β_{dch} Discharge power regulation coefficients

5 η_{inv} Inverter efficiency [%]

Round-trip efficiency of the VRFB system [%]

⁷ C^{im}, C^{ex} Import/export cost from/to utility grid [A\$/kWh]

8 E_n Nominal energy [kWh]

Power consumption of battery's auxiliary system [kW]

10 P^{ch}, P^{dch} Charge/discharge power to/from battery [kW]

 P_{max}^{ch} , P_{max}^{dch} Maximum charge/discharge power to/from battery [kW]

 P_{min}^{ch} , P_{min}^{dch} Minimum charge/discharge power to/from battery [kW]

Import/export power from/to utility grid [kW]

14 P^{load} Load power [kW]

Solar PV generation power [kW]

16 u^{ch} , u^{dch} Battery charge/discharge status

Multi-physics VRFB model

18 $\eta_{con}^+, \eta_{con}^-$ Positive/negative half-cell concentration overpotentials [V]

19 η_{rt} Round-trip efficiency [%]

20 κ_{φ} Membrane electro-kinetic permeability [m²]

Electrode hydraulic permeability [m^2]

Membrane hydraulic permeability [m^2]

 λ_{KC} Kozeny-Carman constant

Positive/negative electrolyte viscosity [Pa · s]

Mean viscosity of electrolyte [Pa · s]

²⁶ ϕ^m_{diff} Effective diffusion potential [V]

27 $\phi_{pos}^m, \phi_{neg}^m$ Ionic potential at positive/negative sides [V]

Electrolyte density [kg m⁻³]

Effective conductivity of the membrane [S m⁻¹]

 $_{2}$ ε Electrode porosity

 $\vec{v}_{electro-osmosis}$ Electrolyte velocity driven by electro-osmosis across membrane [m s⁻¹]

Electrolyte velocity across membrane [m s⁻¹]

5 $\vec{v}_{osmosis}$ Electrolyte velocity driven by osmosis across membrane [m s⁻¹]

6 A_e Cross-sectional area of porous electrode [m²]

Membrane surface area [m²]

8 A_t Surface area of the tank [m²]

Concentration of V^{i+} in the stack [mol m⁻³]

Concentration of V^{i+} in the tank [mol m⁻³]

Fixed acid concentration [mol m⁻³]

Hydrogen ion concentration [mol m⁻³]

Specific heat capacity of electrolyte [J kg⁻¹ K⁻¹]

Total concentration of V^{i+} [mol m⁻³]

Thickness of the membrane [m]

 d_f Fibre diameter [m]

Equilibrium open-circuit potential of the cell [V]

 E^{OCV} Open-circuit voltage [V]

 $E_p^{0'}, E_n^{0'}$ Equilibrium open-circuit potential of the positive/negative half-cell [V]

20 $E_{oc,p}$, $E_{oc,n}$ Open-circuit potential of the positive/negative half-cell [V]

Stack voltage [V]

Faraday's constant [C mol⁻¹] H_e Height of the electrode [m]

24 I Current [A]

Diffusion coefficient of H⁺ [m² s⁻¹] k_i Diffusion coefficient of Vⁱ⁺ [m² s⁻¹]

Length of the electrode [m]

Number of cells in the stack N

29 n_i^{con} Convection fluxes of Vⁱ⁺ [mol m⁻² s⁻¹]

overall crossover fluxes of V^{i+} [mol m⁻² s⁻¹]

₂ n_i^{diff} Diffusion fluxes of Vⁱ⁺ [mol m⁻² s⁻¹]

Electro-migration fluxes of V^{i+} [mol m⁻² s⁻¹]

4 P_{self} Self discharge losses [W]

⁵ Q_c Electrolyte flow rate in cell [m³ s⁻¹]

Rebalance electrolyte flow rate [$m^3 s^{-1}$]

⁷ Q_s Electrolyte flow rate of the system [m³ s⁻¹]

8 R Gas constant [J mol⁻¹K⁻¹]

Overall cell resistance $[\Omega]$

overall stack resistance $[\Omega]$

 SOC, SOC_p, SOC_n State of charge of the system, positive and negative half-system [%]

State of energy [%]

13 T_p , T_n Electrolyte temperature at positive/negative tank [K]

 T_s Electrolyte temperature in the stack [K]

15 T_{air} Air temperature [K]

Heat transfer capability of tank [J K⁻¹ s⁻¹ m⁻²]

Electrolyte volume in the positive/ negative tank [m^3]

Electrolyte volume in the stack $[m^3]$

Width of the electrode [m] W_e

z Number of electrons involved in the redox reactions

Valency of i-th vanadium ions z_i

2 Room temperature model

Heat loss percentage of pumps and inverters [%]

24 \dot{Q}_{ac} Cooling energy by air-conditioner [J]

 $\dot{Q}_{cool}, \dot{Q}_{heat}, \dot{Q}_{loss}$ Cooling, heat generation and heat exchange loss energy [J]

Angular frequency and phase [rad s⁻¹]

27 φ Angular phase [rad]

²⁸ A_{wall} Total surface of walls [m²]

Heat capacity of air in [J kg⁻¹ K⁻¹]

² EER Energy efficiency ratio

Heat transfer coefficient of concrete [W m $^{-2}$ K $^{-1}$]

4 M_{air} Air mass inside the room [kg]

5 m_{fan} Air mass flow through fan [kg s⁻¹]

Power consumption of the pump and air-conditioner [W]

 $_{7}$ P_{VRFB} VRFB power [W]

8 T_{max} , T_{min} Maximum/minimum outside temperature [°C]

9 T_{room} , T_{out} Internal room/ outside temperature [°C]

1. Introduction

11

13

18

19

20

21

22

23

25

26

27

33

34

It is well known that to achieve global greenhouse gas emission reduction targets, we need to deploy renewable energy sources (RESs) at an unprecedented rate throughout the world to replace existing fossil fuel power plants. However, due to the variable and intermittent nature of RES, there is a need for short-, medium-, and long-term energy storage systems to ensure the safe operation of electricity grids and provide consistent quality power to end users. Among the different energy storage technologies, the vanadium redox flow battery (VRFB) is recognised as a practical solution due to its stable performance, low levelized cost of energy (LCOE) and long lifespan with almost no degradation over 20 years [1]. However, without a well-designed battery management system (BMS), the anticipated high performance of VRFBs might not be achievable. Thus, innovative designs for VRFB-BMSs are becoming increasingly important to manufacturers who want to improve the reliability and performance of their products [2].

A significant amount of research and development has been conducted on BMS for nonaqueous batteries, mainly Li-ion batteries, within both the academic and industrial sectors. However, because of different operational principles and designs of aqueous batteries, certain aspects of these BMSs must be redesigned for VRFBs. Unfortunately, the development of VRFB-BMS has so far received limited attention compared to other mainstream battery energy storage systems (BESS) technologies, which has significantly impeded its development. Trovo and Guarnieri et al. [3, 4] provided a detailed BMS design for a 9 kW/27 kWh industrial-scale VRFB (IS-VRFB), covering both hardware and software aspects. Later, Vishnu et al. [5] proposed a BMS design for standalone VRFB applications. To the best of our knowledge, these are the few publications available on the detailed design and implementation of a VRFB-BMS. While these two papers provide detailed and comprehensive descriptions of the VRFB-BMS hardware and software design, they did not thoroughly introduce or explain the working principles and framework of the BMS. For example, they do not provide a mechanism to control the VRFB operational modes or to estimate the critical states of the system for monitoring within the BMS. A review of other studies linked to VRFB-BMS reveals a clear roadblock to development progress, namely the lack of effective tools to manage and operate the battery. For instance, current VRFB-BMS designs overlook issues related to state of charge (SOC) imbalance in half-cells

and lack comprehensive thermal management mechanisms, often only considering standby thermal management [6]. Moreover, most of the work on estimating half-system SOC and optimising flow rates has proposed complex algorithms that exceed real-world computational capabilities of BMSs. As such, we believe developing a practical VRFB-BMS design for commercial- and industrial-scale VRFBs requires significantly more attention.

Another profound concern arises from the absence of robust VRFB-BMS, where most research studies do not consider the true operational dynamics of VRFBs in their design. For instance, while the operation of a VRFB can be divided into charging, discharging, standby, and shutdown modes, most of the reported studies only evaluated proposed BMS design and operational optimisation methods under continuous charge-discharge operation, neglecting standby and shutdown modes. In addition, the existing BMS and operational strategies were not validated under a comprehensive battery management framework, and therefore their feasibility in actual operation remains questionable. For example, all existing model-based flow rate methods assumed that the system states (SOC, vanadium species concentration, electrolyte temperature, etc.) are accurately measured, and so the information from the model was used directly. However, obtaining accurate system states is difficult in an industrial- or commercial-scale VRFB system. As a result, it is of great urgency to develop a well-designed and comprehensive VRFB-BMS scheme that incorporates detailed battery information and a completed design framework for researchers and operators to validate their proposed battery management methods in the context of actual field implementation.

Additionally, like other battery technologies, a VRFB is typically integrated into a larger hybrid power system controlled by an energy management system (EMS). The main goal of an EMS is to maximise the economic benefits of the entire system, including installed BESSs, as a high-level optimisation and control system. If the EMS is not designed based on predefined rules, it continuously solves an optimisation problem at specific intervals for a specified future period to determine the operating points of all assets in the energy system. To this end, a suitable VRFB model should be integrated with the EMS, ensuring that it can be solved both reliably and quickly within an optimisation problem. This is an area where VRFB research is largely lacking, indicating the need for more studies and development [1]. Sumitomo Electric [7] demonstrated a microgrid project with Taiwan Power Research Institute that installed a 125 kW/750 kWh VRFB, a 150 kW PV system, a 50 kW generator system, a 10 kW wind turbine, and a 150 kW load. The entire energy system is managed by a central EMS which demonstrates its practical application in grid-level applications to accomplish different objectives.

In addition, VRFB thermal management is a critical part of the BMS design but has received little attention from the research community. Tang et al. [8] studied standby thermal behaviour to highlight the significance of the choice of cooling flow rate to reduce cumulative heat generation inside the stack. Trovo et al. [6] expanded on this to develop a standby thermal management system for a kW-level VRFB system. However, their cooling flow rate mechanism was only practical in reducing the electrolyte temperature difference between the tank and the stack during the standby period, which is not ideal for cooling the entire VRFB system. VRFB manufacturers appear to prefer standard heating, ventilation, and air conditioning (HVAC) systems as an effective tool for passive cooling of VRFB systems [9]. Furthermore, recent studies by Wang et al. [10] and Shu et al. [11] provided two different case studies using HVAC for thermal management and validated its effectiveness. However, at this stage, there is no comprehensive thermal management design for VRFB systems that considers the cooling flow rate and passive cooling by HVAC under real-world load, temperature and operational conditions, which should be considered in future development. In summary, our literature review reveals a lack of effective and

efficient VRFB-BMS design, especially with respect to SOC estimation, thermal management, and integration of a BMS into an EMS.

To address these research gaps, this study introduces an advanced VRFB-BMS to overcome the limitations of existing VRFB-BMS designs. This study is conducted using a new zero-dimensional model (0-D) that incorporates all crossover and electrolyte transfer mechanisms and thermal dynamics of VRFBs. The key contributions and features of the proposed BMS presented in this paper are outlined below:

- A comprehensive and practical VRFB-BMS design is proposed, which is computationallyefficient for industrial and commercial-scale hardware design. The detailed design and
 working principles are given and evaluated in this paper.
- Four operational modes (charge/discharge/stop/standby) are considered in the BMS design
 to simulate the on-site operation of the VRFB systems. This provides useful information
 for researchers in the field to rigorously evaluate their proposed methods considering the
 operational dynamics of VRFB systems.
- High-performance and computationally-efficient half-system SOC estimation model, and flow rate control and automatic electrolyte rebalancing methods are proposed and rigorously validated in this work.
- A hybrid HVAC and flow rate cooling strategy is proposed to conduct energy-efficient and effective thermal management for VRFB systems.

The rest of this paper is organised as follows. In Section 2, a 0-D multi-physics VRFB model with thermal modelling is presented, which is developed based on the works by Wang et al. [12, 10], that incorporates all ion crossover and electrolyte transfer mechanisms with battery configurations. Rigorous validations for the 5 kW VRFB system are carried out in Section 3. The functionalities and critical battery management functions are explained in Section 4 and the integration of these functions into a comprehensive and advanced VRFB-BMS design. Lastly, real data are used to test the effectiveness of the proposed VRFB-BMS design in thermal management, accurate SOC estimation, energy savings, and capacity recovery are presented in Section 5.

28 2. Multi-physics vanadium redox flow battery model

VRFB systems are normally used as medium- or large-scale BESSs for residential or grid-level applications. In Fig. 1, a general schematic of a large-scale VRFB system composed of two electrolyte storage tanks, a compact battery stack, two electrolyte circulation pumps, and piping systems. The main chemical reactions take place inside the cells in the stack. These chemical reactions in the positive/negative half cells and the overall cell reaction are:

Negative half-cell reaction:

$$V^{3+} + e^{-} \underset{\text{Discharge}}{\overset{\text{Charge}}{\rightleftharpoons}} V^{2+} \tag{1}$$

Positive half-cell reaction:

q

$$VO^{2+} + H_2O \underset{Discharge}{\overset{Charge}{\rightleftharpoons}} VO_2^+ + 2H^+ + e^-$$
 (2)

Overall cell reaction:

$$VO^{2+} + V^{3+} + H_2O \underset{Discharge}{\overset{Charge}{\rightleftharpoons}} VO_2^+ + V^{2+} + 2H^+$$
 (3)

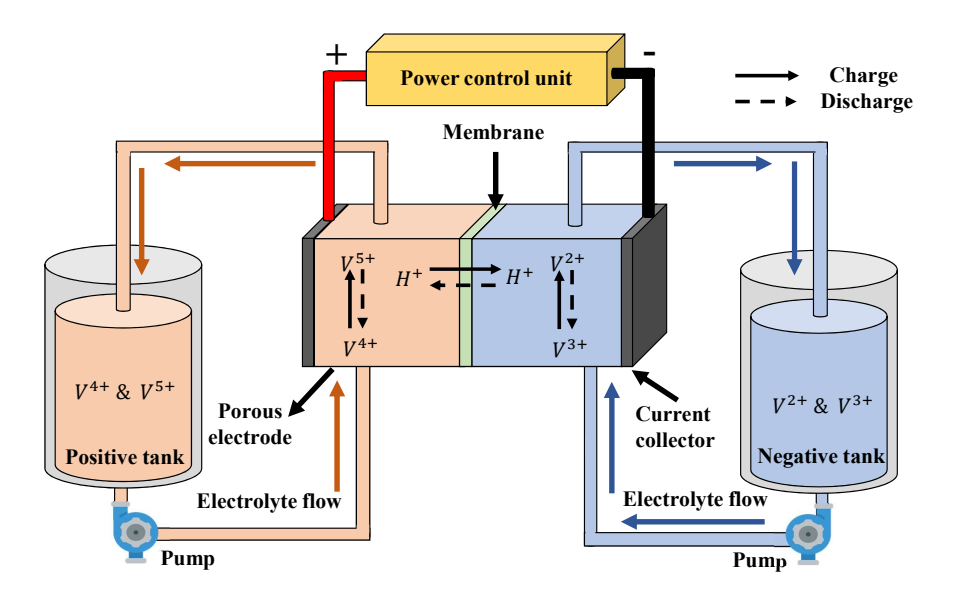


Figure 1: A schematic of a typical VRFB system showing its components and structure [12]

- To comprehensively validate and analyse the performance of the proposed VRFB-BMS for an actual 5 kW VRFB system, a new and rigorously validated multi-physics model was utilised in this study for validation and in-depth analysis. This model incorporates all types of crossover and electrolyte transfer mechanisms. The basic assumptions for this model are:
- The gas evolution (hydrogen and oxygen) and membrane degradation are not considered in this study as these can be minimised by good battery design [13].
 - It is assumed that the vanadium ions are perfectly mixed and uniformly distributed in the two tanks and stack [13, 14, 15].
 - The stack overall resistance remains constant during the operation [14].
 - The flow channel and hydraulic system of the stack are well designed and thus the effect of the shunt current is minor and can be ignored [13, 14, 15].
 - The electrolyte volume difference between the half cells is caused by electrolyte transfer [12].

2.1. Mass balance model

10

11

12

13

14

15

A mass balance model is developed to simulate the vanadium ion crossover effect driven by the concentration gradient, electric field, and osmotic pressure across the membrane [12]. The diffusion flux, osmotic pressure flux, and electro-migration flux are derived using the following equations:

$$n_i^{diff} = k_i \frac{c_i}{D} \tag{4}$$

$$n_i^{con} = \vec{v}_m \ c_i \tag{5}$$

$$n_i^{mig} = \frac{z_i F}{RT} k_i c_i \nabla (\phi_{neg}^m - \phi_{pos}^m)$$
 (6)

Note that n_i^{diff} , n_i^{con} and n_i^{mig} represent the diffusion fluxes, convection fluxes, and electromigration fluxes correspondingly. The overall crossover flux is given as:

$$n_i^{cross} = n_i^{diff} + n_i^{con} + n_i^{mig} \tag{7}$$

For the vanadium ions in the cell:

$$\frac{dc_2^s}{dt} = \frac{Q_c \left(c_2^t - c_2^s\right) \pm \frac{I}{zF} - n_2^{cross} A_m - 2n_5^{cross} A_m - n_4^{cross} A_m}{L_e W_e H_e}$$
(8)

$$\frac{dc_3^s}{dt} = \frac{Q_c \left(c_3^t - c_3^s\right) \mp \frac{I}{zF} - n_3^{cross} A_m + 3n_5^{cross} A_m + 2n_4^{cross} A_m}{L_e W_e H_e} \tag{9}$$

$$\frac{dc_4^s}{dt} = \frac{Q_c \left(c_4^t - c_4^s\right) \mp \frac{I}{zF} - n_4^{cross} A_m + 3n_2^{cross} A_m + 2n_3^{cross} A_m}{L_e W_e H_e}$$
 (10)

$$\frac{dc_5^s}{dt} = \frac{Q_c \left(c_5^t - c_5^s\right) \pm \frac{I}{zF} - n_5^{cross} A_m - 2n_2^{cross} A_m - n_3^{cross} A_m}{L_e W_e H_e}$$
 (11)

For the vanadium ions in the tanks:

$$(V_n + N \Delta V_n) \frac{dc_2^t}{dt} = Q_s \left(c_2^s - c_2^t\right)$$
(12)

$$(V_n + N \Delta V_n) \frac{dc_3^t}{dt} = Q_s \left(c_3^s - c_3^t\right) \tag{13}$$

$$(V_p + N \Delta V_p) \frac{dc_4^t}{dt} = Q_s \left(c_4^s - c_4^t \right) \tag{14}$$

$$(V_p + N \Delta V_p) \frac{dc_5^t}{dt} = Q_s \left(c_5^s - c_5^t\right) \tag{15}$$

Note that in Eqs. (16)-(19), the electrolyte transfer mechanism is taken into account in the dynamic model, where ΔV_p and ΔV_n are the electrolyte transfer rates. Assuming an a hydraulic shunt is used for electrolyte rebalancing, the vanadium ions and electrolyte volume variations in the tanks during the rebalancing process are:

$$(V_n + N \Delta V_n + Q_{rb} \Delta t) \frac{dc_2^t}{dt} = Q_s \left(c_2^s - c_2^t \right) + Q_{rb} \left(-c_4^t - 2c_5^t \right)$$
 (16)

$$(V_n + N \Delta V_n + Q_{rb} \Delta t) \frac{dc_3^t}{dt} = Q_s \left(c_3^s - c_3^t \right) + Q_{rb} \left(2c_4^t + 3c_5^t \right)$$
 (17)

$$(V_p + N \Delta V_p - Q_{rb} \Delta t) \frac{dc_4^t}{dt} = Q_s \left(c_4^s - c_4^t \right) - Q_{rb} c_4^t$$
 (18)

$$(V_p + N \Delta V_p - Q_{rb} \Delta t) \frac{dc_5^t}{dt} = Q_s \left(c_5^s - c_5^t \right) - Q_{rb} c_5^t$$
 (19)

- 1 2.1.1. Electrolyte volume modelling
- The continuous electrolyte transfer from the negative side to the positive side is mainly driven
- ₃ by osmotic pressure and ionic potential. The electrolyte velocity across the membrane driven by
- 4 osmotic pressure is given by the following equation [16].

$$\vec{v}_{osmosis} = \frac{\kappa_m}{D} \cdot \frac{L_e}{2\kappa_e A_e} \cdot \left(Q_c - \frac{\mu^+}{\mu^-} Q_c \right)$$
 (20)

Note that κ_e is the permeability of the porous electrode which is given by:

$$\kappa_e = \frac{d_f^2}{16\lambda_{KC}} \frac{\varepsilon^3}{(1 - \varepsilon)^2} \tag{21}$$

The electrolyte velocity driven by the electro-osmotic is given by [17]:

$$\vec{v}_{electro-osmosis} = -\frac{\kappa_{\varphi}}{\mu_{w}} c_{f} F \left(\frac{I}{\sigma_{m} A_{m}} + \phi_{diff}^{m} \right)$$
 (22)

where σ_m is the conductivity of the membrane, which is given by [18]:

$$\sigma_m = \frac{F^2}{RT} \sum_i z_i^2 c_i k_i \approx \frac{F^2}{RT} c_{H^+} k_{H^+}$$
 (23)

The effective diffusion potential ϕ_{diff}^m is given as follows [19]:

$$\phi_{diff}^{m} = \frac{F \sum z_{i} k_{i}^{m} \nabla c_{i}^{m}}{\sigma_{m}}$$
 (24)

$$\vec{v}_m = \vec{v}_{electro-osmosis} + \vec{v}_{osmosis} \tag{25}$$

As a result, the derivation of the electrolyte volume transfer rate is given below:

$$\Delta V_n = (\vec{v}_{electro-osmosis} + \vec{v}_{osmosis}) A_m \tag{26}$$

$$\Delta V_p = -\left(\vec{v}_{electro-osmosis} + \vec{v}_{osmosis}\right) A_m \tag{27}$$

10 2.2. Thermal modelling

The thermal behaviour of the 5 kW/10 kWh VRFB system is modelled based on the energy conservation law presented in [10]. The model of the electrolyte temperature in the stack consid-

ers the self-discharge reactions, entropy variations, internal heat generation, and electrolyte heat exchange, and its derivation is given by:

$$C_{p\rho}V_{s}\frac{dT_{s}}{dt} = Q_{s}C_{p\rho}\left(T_{p} - T_{s}\right) + Q_{s}C_{p\rho}\left(T_{n} - T_{s}\right) + I^{2}r_{s} + IT_{s}\frac{dE}{dT} + P_{self}$$

$$\tag{28}$$

The electrolyte temperature in the positive/negative tanks can be determined from the equations:

$$C_p \rho V_p \frac{dT_p}{dt} = Q_s C_p \rho \left(T_s - T_p \right) + U_t A_t \left(T_{air} - T_p \right) \tag{29}$$

$$C_p \rho V_n \frac{dT_n}{dt} = Q_s C_p \rho \left(T_s - T_n \right) + U_t A_t \left(T_{air} - T_n \right)$$
(30)

Note that in this study, the minor heat friction by the electrolyte is not considered following the assumption made by Tang et al. in [8] to reduce the complexity of the thermal model. Furthermore, the difference in the electrolyte volume between the positive/negative tanks may result in a difference in the results of the electrolyte temperature in these two tanks. However, from the experimental results of Trovo et al. in [20], it can be seen that the electrolyte temperature difference between the two tanks is negligible. In this work, considering the difficulties of modelling the electrolyte heat exchange across the membrane because of the electrolyte temperature difference between the half-cells, the small volume difference between the tanks is ignored in the thermal model, which results in a uniform electrolyte thermal distribution. This assumption is reasonable considering that the 5 kW/10 kWh VRFB system used in this study has a hydraulic shunt to rebalance the electrolyte volume. This will minimise the electrolyte volume difference in the two half-systems. More details and explanations of the thermal model can be found in [10].

2.3. Electrochemical model

19

25

In this section, an electrochemical model of VRFB is developed to simulate the stack voltage performance of the 5 kW/10 kWh VRFB system. The open circuit voltage (OCV) of a single cell can be formulated as [21]:

$$E^{OCV} = E^{0'} + \frac{RT}{zF} \ln \left(\frac{c_2^s c_5^s}{c_3^s c_4^s} \right); E^{0'} = 1.40 \text{ V}$$
 (31)

The total stack voltage can be represented as the sum of the overpotentials and the OCV, as indicated below for charging [21]:

$$E_{s} = N \left[E^{0'} + \frac{RT}{zF} \ln \left(\frac{c_{2}^{s} c_{5}^{s}}{c_{3}^{s} c_{4}^{s}} \right) + Ir' - \frac{RT}{zF} \ln \left(1 - \frac{I}{k_{m} F L_{e} H_{e} c_{3}^{s}} \right) - \frac{RT}{zF} \ln \left(1 - \frac{I}{k_{m} F L_{e} H_{e} c_{4}^{s}} \right) \right]$$
(32)

The stack voltage during discharging is:

$$E_{s} = N \left[E^{0'} + \frac{RT}{zF} \ln \left(\frac{c_{2}^{s} c_{5}^{s}}{c_{3}^{s} c_{4}^{s}} \right) - Ir' + \frac{RT}{zF} \ln \left(1 - \frac{I}{k_{m} F L_{e} H_{e} c_{5}^{s}} \right) + \frac{RT}{zF} \ln \left(1 - \frac{I}{k_{m} F L_{e} H_{e} c_{5}^{s}} \right) \right]$$
(33)

$$k_m = 1.6 \times 10^{-3} \left(\frac{Q_c}{10 L_e W_e} \right)^{0.4} \tag{34}$$

Note Eq. (34) is used to derive the mass transfer coefficient k_m in dm s⁻¹ [12], and in this form the units for Q_c , L_e and W_e are L s⁻¹, dm and dm, correspondingly. The SOC is estimated

Table 1: Model parameters and their definitions of the 5 kW/10 kWh VRFB system [12, 22, 16, 23, 24, 25, 26]

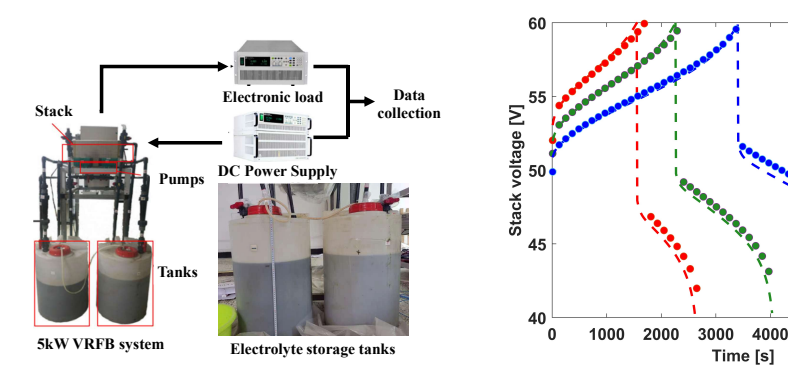
Symbol	Definition	Value
N	Number of cells in the stack	37
c	Total concentration of vanadium ions in mol L ⁻¹	1.5
$\overline{V_n}$	Volume of the electrolyte in the negative tank in L	240
$\overline{V_p}$	Volume of the electrolyte in the positive tank in L	240
H_e	Height of the electrode in m	0.3
L_e	Length of the electrode in m	0.7
$\overline{W_e}$	Width of the electrode in m	2.5×10^{-3}
A_m	Membrane area in m ²	0.21
\overline{D}	Thickness of the membrane in m	1.27×10^{-4}
T	Ambient temperature in K	298.15
R	Gas constant in J mol ⁻¹ K ⁻¹	8.314
$\frac{\rho}{F}$	Electrolyte density in kg m ⁻³	1300
F	Faraday's constant in C mol ⁻¹	96,485
r'	Overall cell resistance in Ω	1.3×10^{-3}
$\overline{k_2}$	Diffusion coefficient of V ²⁺ in m ² s ⁻¹	8.768×10^{-12}
	Diffusion coefficient of V ³⁺ in m ² s ⁻¹	3.222×10^{-12}
k ₄	Diffusion coefficient of V ⁴⁺ in m ² s ⁻¹	6.825×10^{-12}
k5	Diffusion coefficient of V ⁵⁺ in m ² s ⁻¹	5.897×10^{-12}
k_{H^+}	Diffusion coefficient of H ⁺ in m ² s ⁻¹	3.35×10^{-9}
A	Cross sectional area of the porous electrode in m ²	7×10^{-4}
$\overline{d_f}$	Fibre diameter in m	1.76×10^{-5}
ε	Electrode porosity	0.93
λ_{KC}	Kozenye-Carman constant	4.28
Km	Membrane hydraulic permeability in m ²	2×10^{-19}
κ_{φ}	Membrane electro-kinetic permeability in m ²	1.13×10^{-20}
μ_w	Mean viscosity of the bulk electrolyte in Pa · s	4.2×10^{-3}
	Fixed acid concentration in mol L ⁻¹	2.5
$\frac{c_f}{C_p}$ A_t	Specific heat capacity of electrolyte in J g ⁻¹ K ⁻¹	3.2
A_t	Surface area of the tank in m ²	2.8
$\overline{U_{t}}$	Overall heat transfer capability of the tank in J K ⁻¹ s ⁻¹ m ⁻²	3.67
ρ	Electrolyte density in g cm ⁻³	1.354

considering the imbalance between the half-systems, by the following equation [27]:

$$SOC = \min\left(\frac{c_2^t}{c_2^t + c_3^t}, \frac{c_5^t}{c_4^t + c_5^t}\right)$$
 (35)

2 3. Model validation

This study uses an industrial-scale 5 kW/3 kWh VRFB system and extends into a 5 kW/10 kWh VRFB system for case studies and validation. This is done to verify the effectiveness of VRFB-BMS in actual residential settings, as 10 kWh is a common battery size for residential BESSs. Because VRFB systems allow for independent power and energy ratings, increasing the rated energy can be easily accomplished by adding more electrolyte to the tanks. The schematic of the original VRFB system is shown in Fig. 2 (a), where each half tank contains 70 L of electrolyte from the measurement. Although the electrolyte volume in each half tank of the 5 kW/10 kWh system is increased to achieve higher energy capacity, other parameters of the



(a) Schematic of the 5 kW/3 kWh experimental VRFB sys- (b) Stack voltage comparison (under 60~A,~80~A and tem 100~A currents)

100A(Sim) 100A(Exp) 80A(Sim)

80A(Exp)

60A(Sim) 60A(Exp)

5000 6000

Figure 2: Schematic of the 5 kW/3 kWh experimental VRFB system and model validation results under three different currents [12]

original 5 kW/3 kWh VRFB system remain the same, as reported in Table 1. With an identical stack design, the hydraulic pressure drop and pump power consumption profile will also be consistent with those reported in [22].

Experimental data for the initial 5 kW/3 kWh VRFB stack were obtained from a VRFB setup experiment employing LabView at a room temperature of 25°C under constant operational currents of 60 A, 80 A and 100 A [22]. The cut-off voltage limit was 40-60 V, the initial SOC in each operational current regime was 10% and the electrolyte flow rate was 1 m³/h. The data has then been used in [22] to validate the accuracy of the proposed model. Note in this study, the value of membrane hydraulic permeability is increased compared with the value in [12] to exhibit a more rapid electrolyte volume transfer rate for electrolyte volume rebalance validation in the later section. Fig. 2 (b) presents the model validation results in this work, which demonstrate accurate estimations with mean absolute error (MAE) and mean absolute percentage error (MAPE) less than 1 V and 2%, correspondingly for these three different current regimes.

4. Battery management system functionalities and design

4.1. Systematic VRFB-BMS design

10

17

18

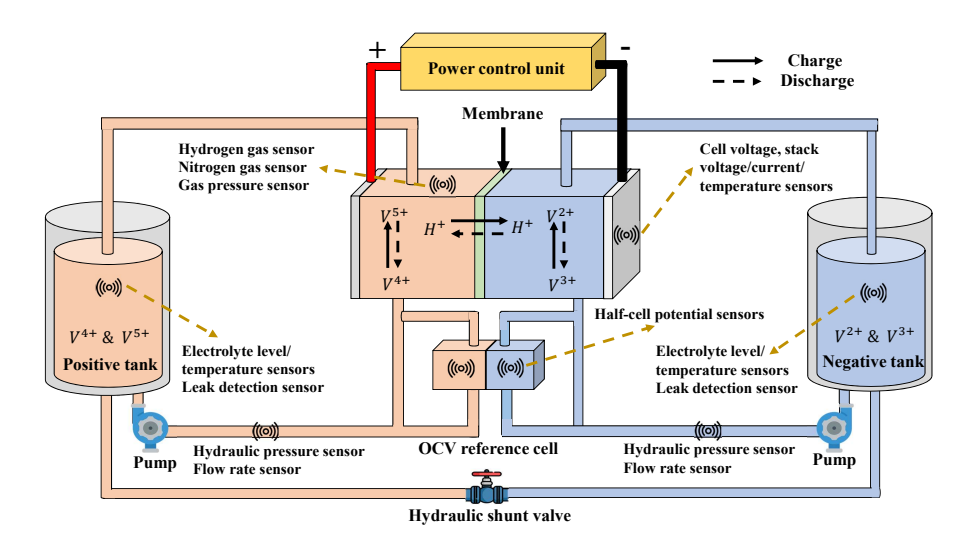
19 20

21

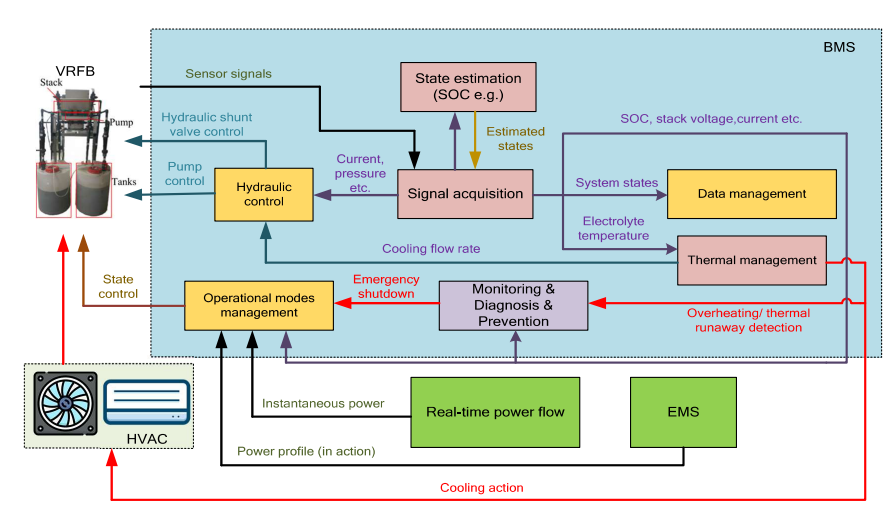
22

The primary objective of a BMS is to protect, manage and optimise battery operation to satisfy the energy demand of end users. At the same time, an efficient and functional VRFB-BMS design should avoid computationally intensive algorithms or methods to ensure rapid and cost-effective performance in industrial or commercial VRFB systems, as indicated by Trovo et al. [3].

To effectively and efficiently manage VRFBs, sensors are crucial as they offer real-time measurements of various key states, thus aiding in the monitoring and control during battery operation. In our VRFB-BMS design, we propose installing different sensors to monitor critical systems state parameters, including SOC, voltage, current, and pressure drop. The type and location of these sensors proposed to be embedded in the 5 kW/10 kWh VRFB system are shown in the schematic diagram of Fig. 3 (a). More details on the types of sensors and their functionalities



(a) The proposed location of sensors used in the VRFB system design



(b) Proposed VRFB-BMS scheme integrated within an EMS

Figure 3: The illustration of the proposed sensors placement in the VRFB-BMS design and their intended functionalities

- in contemporary VRFB systems are given in Table 2. Building on [1], an advanced VRFB-BMS framework with seven main functionalities was proposed. This study integrates these critical
- ³ functionalities into the proposed VRFB-BMS architecture, providing concrete technical specifi-
- 4 cations.
- In applications such as energy arbitrage, the operational decisions of BESSs are determined by an upper-level EMS. Usually, an EMS gathers information from the current state of the power
- y systems, e.g., electricity prices, end-user load demand, renewable energy generation, and their

Table 2: Typical sensors used in the design of a VRFB-BMS and their functionalities

Sensors	Functionality	Ref.			
Stack					
Flow channel pressure drop	Measure the pressure drop in the stack	[28]			
Stack voltage	Measure the overall stack voltage.	[3]			
Stack current	Measure the stack current.	[3]			
Stack temperature	Measure the electrolyte temperature in the stack.	[28]			
Cell voltage	Measure the cell voltage.	[28]			
Tanks					
Hydraulic pressure	Measure the pressure drop on the half-systems.	[3]			
Flow rate	Measure the flow rates on the half-systems.	[3]			
Electrolyte level	Measure the electrolyte level of the two tanks.	[3]			
Electrolyte temperature	Measure the electrolyte temperature inside the two tanks.	[3]			
Half-potential	Measure the half-cell potentials for SOC estimation.	[3]			
Leak detection	Detect the electrolyte leakage.	[29]			
Hydrogen/nitrogen gas	Detect the gas generation.	[29]			
Gas pressure sensor	Measure the gas pressure.	[29]			

future forecasts. Using these crucial pieces of information, typically an optimisation problem is solved, and the optimal decisions are communicated to other different system components. In the case of a BESS, the commands go through the inverter for implementation in connection with the BMS. The primary task of the BMS is to perform localised management to ensure safe and stable battery operation. Despite the predominant focus on localised online management in most current BMS designs, the emerging trend emphasises that a cooperative strategy between the BMS and an EMS can improve the economic benefits of BESSs in different applications.

10

19

20

22

24

26

27

A block diagram of the VRFB-BMS design with these functionalities is shown in Fig. 3 (b). As indicated in this figure, it is designed to manage and process the power schedule from the upper-level management system, while it also achieving local management in real-time operation. The primary objective of a VRFB-BMS is to detect and control operational modes according to the scheduled power profile or the real-time power flow to decide when the VRFB system should be charged, discharged, in standby mode, or shut down. During operation, the BMS in Fig. 3 first collects sensor data and processes it to estimate certain system state parameters that are not directly observable, such as SOC. The measured and estimated system states are transmitted to different functional modules via the signal acquisition unit for battery management. Note that some BMSs have a data management module to save and process historical data for analysis, and this data is typically stored in the cloud for future research and product development by the manufacturers. To avoid unnecessary complexity, we do not show the data management unit in the block diagram. The hydraulic control module and thermal management module receive these transmitted signals from the BMS to control the flow rate, rebalance the electrolytes, and detect/prevent thermal issues. Addressing issues of overheating and thermal runaway is crucial to mitigate capacity fading in VRFB systems caused by thermal precipitation. The thermal management system can effectively regulate cooling flow rates during standby periods or use the heating, ventilation, and air conditioning (HVAC) system throughout charging and discharging periods. If the monitored battery state reaches the predefined cut-off limits, the BMS will switch to standby mode to prevent overcharging or over-discharging. However, if severe incidents occur that exceed the emergency limits, the VRFB system will immediately shut down the battery. Such urgent situations may include instances of system-wide overheating or the detection of electrolyte leakage by the electrolyte level sensors.

4.2. Battery operational modes control

The switching of battery modes is the key to achieving its function based on the requirements of site operations. In Fig. 4, the systematic control of the operational mode within the BMS is presented. The VRFB system starts operation either when the scheduled start-up time is reached or through manual activation. Note that, because of the different designs of VRFB, the electrolytes in some of these VRFB systems will be stored in two separate storage tanks before shutdown. For VRFB systems with this particular design, it is necessary to have a pre-startup sequence by activating pumps on both ends to fill the stacks with electrolytes. For VRFB designs in which the electrolyte remains in the stack, it is still essential to use a high electrolyte flow rate to quickly circulate the electrolyte when a load is applied. This is designed to prevent gas evolution and other side reactions that could lead to capacity fading and subsequent issues with overcharging or over-discharging. Once the VRFB system is activated by the start command, the monitoring and surveillance systems are initialised to manage battery operation. Meanwhile, the signal acquisition and state estimation modules start to continuously monitor or estimate battery states and communicate the results to other modules for use.

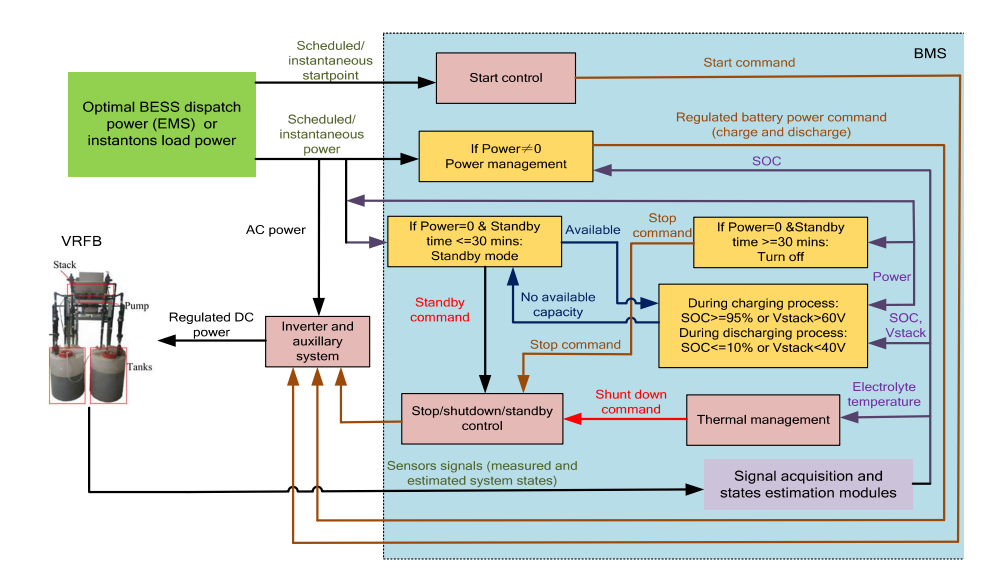


Figure 4: The mode control flow chart for the 5 kW/10 kWh VRFB system integrated with EMS or other external high-level control platforms

After the BMS is activated, the power management function begins to control the battery's operational modes in real-time. For instance, if the scheduled/instantaneous power is negative/positive/zero, the battery will go into charge/discharge/standby mode, respectively. However, due to the cut-off thresholds designed to protect the VRFB system from overcharging and over-discharging that could threaten the lifespan and thermal stability of the VRFB, the power flow will stop and the battery will go into standby mode once the stack voltage (40-60 V) and SOC (10-95%) reach cut-off limits. In this design, the BMS shuts the system down and, if appropriate, discharges the electrolytes inside the stack into separate tanks if there is a scheduled standby period of over 30 minutes. This is to avoid rapid self-discharge by the ion crossover

inside each cell. Note that the thermal management unit will shut down the VRFB system once the electrolyte temperature in the stack or tank reaches 50°C in this design.

4.3. State of charge monitoring

10

11

12

16

17

19

20 21

22

23

26 27

29

31

32

37

The SOC is a vital indicator used in the BMS to estimate the remaining battery capacity and knowledge of this parameter is critical to ensure safe and efficient battery operation [30]. In order to achieve highly accurate SOC estimation, a significant amount of effort has been focused on the development of SOC observers, mainly using the Kalman filter and its extensions. However, two significant obstacles hinder the advancement of these observer-based methods in VRFB-BMS and other BMS applications. The first obstacle is that SOC observers must be designed on a relatively accurate state-space model. However, some critical parameters in the VRFB models, such as the membrane permeability and electrode porosity dimensions, are sensitive to the operating conditions (e.g., temperature variations, degradation levels, etc.) or difficult to measure or obtain from the manufacturer's datasheets. Furthermore, SOC observers are designed based on relatively simple 0-D models without considering vanadium ion crossover mechanisms (the crossover driven by the electric field and membrane osmotic pressure) [31, 32]. As a result, they offer limited accuracy in a large number of operational cycles. Although some adaptive filters have been proposed to handle the limitations mentioned above, these advanced observerbased methods normally require substantial computational capacity, which is not available in commercial- or industrial-scale BMS systems. In conclusion, a simple and efficient method is needed to accurately estimate the remaining capacity of positive and negative half cells in VRFB

Moreover, the proposed method for SOC estimation must be robust enough to mitigate electrolyte imbalances arising from extended operational periods and to accurately estimate the SOC in both the negative and positive half-cells. Currently, methods based on coulombic counting (CC) and OCV observation are the most widely used in existing BMS. In the only article that addressed VRFB-BMS [3], a simple OCV-based derivation method was used for SOC estimation, as:

$$SOC = \frac{\exp\left(\frac{zF}{2RT}\left(E^{OCV} - E^{0'}\right)\right)}{1 + \exp\left(\frac{zF}{2RT}\left(E^{OCV} - E^{0'}\right)\right)}$$
(36)

where z, F, R and T are the number of electrons transferred, Faraday's constant, gas constant and electrolyte temperature, respectively. E^{OCV} and $E^{O'}$ are the open-circuit voltage of a single cell and its equilibrium open-circuit potential (OCP) measured at 50% SOC [13]. The value of $E^{O'}$ in this study is 1.40 V, obtained from the experimental results by Li et al. [13]. This equation is based on the assumption that there is no concentration imbalance between the positive and negative sides (e.g., $SOC = SOC_n = SOC_p$). In this scenario, the Nernst equation can be formulated as follows:

$$E^{OCV} = E^{0'} + \frac{2RT}{zF} \ln \left(\frac{SOC}{1 - SOC} \right)$$
 (37)

During the operation of the VRFB system, the imbalance of electrolyte concentration on the positive and negative sides becomes more significant. Simultaneously, the concentration of each vanadium ion on both sides tends to become more disproportional to SOC variations due to their different crossover capabilities, as indicated by the results in [33]. To overcome this problem, Corcuera et al. [34] designed a reference electrode to measure the half-cell potentials.

Later, Ngamsai et al. developed a new middle half-cell inside the conventional OCV reference cell [35]. Rigorous validations are given in [35] to highlight the feasibility of these proposed half-cell designs to measure the system imbalance. In recent studies, exemplified by the work of Li et al. [13], it is evident that the design of reference OCV half-cells has been successfully implemented in a laboratory-scale VRFB system which is a practical solution from the hardware design perspective. The open-circuit potentials for negative and positive half-cells are given below [13]:

$$E_{oc,n} = E_n^{0'} + \frac{RT}{zF} \ln \left(\frac{1 - SOC_n}{SOC_n} \right)$$
 (38)

$$E_{oc,p} = E_p^{0'} + \frac{RT}{zF} \ln \left(\frac{1 - SOC_p}{SOC_p} \right)$$
 (39)

where $E_{oc,n}$ and $E_{oc,p}$ are half-cell OCP for the negative/positive half-systems, and $E_n^{0'}$ and $E_p^{0'}$ are the equilibrium OCP for the negative and positive half-cells measured separately at 50% SOC [13], respectively (0.43 V and -0.97 V from [13]). As a result, the SOC of the negative and positive sides can be derived as [36]:

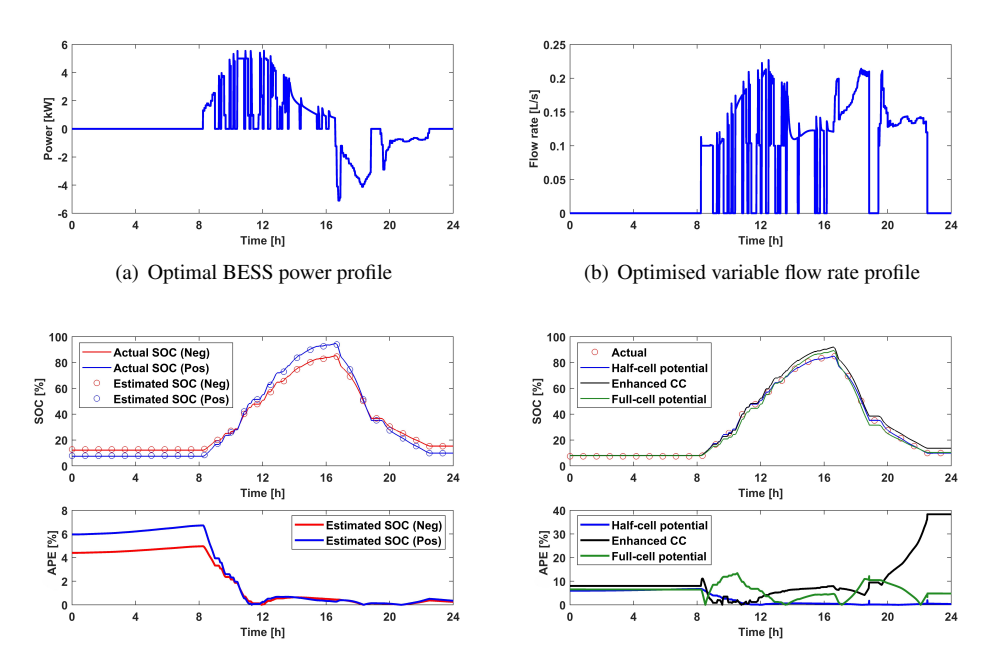
$$SOC_n = \frac{1}{1 + \exp\left(\frac{zF}{RT}\left(E_{oc,n} - E_n^{0'}\right)\right)}$$
(40)

$$SOC_{p} = \frac{\exp\left(\frac{zF}{RT}\left(E_{oc,p} - E_{p}^{0'}\right)\right)}{1 + \exp\left(\frac{zF}{RT}\left(E_{oc,p} - E_{p}^{0'}\right)\right)}$$
(41)

To validate the performance of the proposed half-cell potential for SOC estimation, an optimal BESS power profile is used, which fluctuates considerably due to load demand and rooftop solar variations. This profile is derived from real residential user data in the Australian Capital Territory (ACT), Australia [37]. The variable flow rate, which reduces overall losses, increases the complexity of the VRFB system operation. Additionally, during that day of operation, the 5 kW/10 kWh VRFB system undergoes stop, standby, charge, and discharge modes to replicate real-world conditions. The initial concentration of V^{2+}, V^{3+}, V^{4+} and V^{5+} was set to 0.2, 1.45, 1.25, 0.1 mol/L, respectively, to simulate a severe electrolyte concentration imbalance ($c^{2+} + c^{3+} \neq c^{4+} + c^{5+}$) between these two half-cells and vanadium species concentration imbalance ($c^{2+} + c^{3+} \neq c^{4+} + c^{5+}$) in each half-cell. The performance of the proposed method is evaluated and compared with other mainstream SOC estimation methods in the IS-VRFB system (enhanced CC [36] and full-cell potential estimation method [3]), where the results are given in Fig. 5.

As indicated in Figs. 5 (a) and (b), a varying power profile and optimised flow rates are applied to the 5 kW/10 kWh VRFB system using the proposed 0-D VRFB model in [12] to simulate on-site operation. The actual SOC is obtained using Eq. 5, which considers the concentration imbalance of vanadium species. The results in Fig. 5 (c) indicate that the proposed half-potential SOC measurement technique shows excellent accuracy in estimating the SOC of half-cells with a mean absolute percentage error (MAPE) of less than 0.6%. Moreover, the performance of two popular VRFB SOC estimation methods at the system level is shown in Fig. 5 (d). The two methods are

1. **Enhanced CC method**: Considers the charge/discharge coulombic efficiency from the CC-CV/CC tests [36, 38].



(c) Actual and estimated half-cell SOCs and the absolute (d) Actual and estimated full-system SOCs by different percentage error (APE) mainstream estimation methods and their APE

Figure 5: The performance of the proposed half-cell potential SOC measurement method and other existing methods under the varying BESS power and flow rate profiles over a day

2. **Full-cell potential method**: Another universal open-circuit potential-based method for system SOC estimation measured by the half-cell potential [3].

The results in Fig. 5 (d) show that our proposed method achieves high accuracy compared to the other two methods. The enhanced CC and full-cell potential methods neglect the dynamic ion crossover process during VRFB operation, leading to more significant errors in the SOC estimation outcomes. However, in this study, the variations of the degree of acidity or alkalinity of the electrolyte are neglected due to the relatively high concentration of hydrogen ions in the electrolyte design. For some VRFB electrolyte designs with low acid concentrations, variations in hydrogen ions may result in a lower SOC estimation accuracy using this proposed half-cell potential SOC estimation method. In this case, a more comprehensive exploration of how hydrogen ion concentration influences the cell OCV is essential. Detailed experimental analysis is required to clarify its impact, thereby enhancing the accuracy of the suggested SOC estimation technique.

4.4. Hydraulic shunt control for electrolyte rebalancing

3

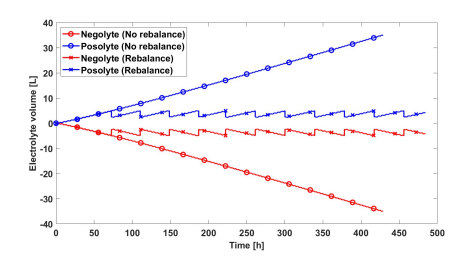
13

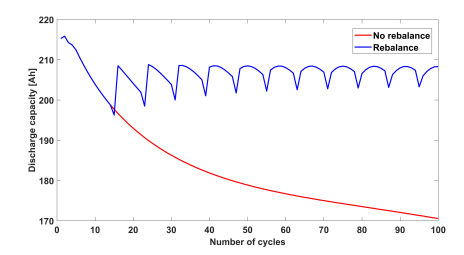
15

16

17

The most competitive and attractive advantage of VRFBs compared to other battery technologies is their long life, as they have almost no degradation over 20-30 years. However, this is only achievable by preventing the oxidation and precipitation of vanadium ions in the electrolyte and ensuring the balance of positive electrolyte (posolyte) and negative electrolyte (negolyte) volumes. For industrial and commercial-scale VRFB systems, sealed tanks with gas bubbler





- (a) The positive/negative electrolyte volume variation profiles
- (b) The actual battery capacity during discharge

Figure 6: The half-system electrolyte volume variation and discharge capacity profile of the 5 kW/10 kWh VRFB system over 100 cycles with a constant operational current of 100 A over 100 cycles with/without automatic rebalancing using hydraulic shunt

systems are the most effective solution to significantly reduce the oxidation of vanadium species [39]. The thermal precipitation of vanadium species is less likely to occur because the electrolyte has a high tolerance to ambient temperature (around 40°C for most VRFB systems) and effective thermal management procedures are carried out to manage ambient temperature.

To restore the capacity by electrolyte volume rebalance, several practical methods have been proposed including remixing of electrolytes [40], electrolyte reflow [41], continuous electrolyte overflow [42] and hydraulic shunts [39]. The hydraulic shunt emerges as the most promising technological solution, which only requires switchable connections at the bottom of the tanks [39]. In this study, the hydraulic shunt is considered using a simple pipe connecting the two electrolyte storage tanks and an automatic valve in the pipe that is controlled by the BMS for periodic rebalancing. Considering the complexity of simulating the density of the negolyte and posolyte due to the concentration variations of different ions, simulating the hydraulic pressure at the two ends of the electrolyte feeding pipe is challenging. Therefore, in this work, it is assumed that upon valve opening, the electrolyte flow rate through the electrolyte feeding pipe is 0.1 L/s. Upon detection of a volumetric disparity exceeding 10 L by electrolyte level sensors within the tanks, the BMS automatically opens the valve in the electrolyte feeding pipe to initiate equilibrium. In contrast, when the volume differential decreases below 5 L, the automatic balancing valve will be closed. In Fig. 6, the simulated performance of the electrolyte rebalance design is given, in which a high constant pump flow rate of 0.8 L/s is used to show a more significant electrolyte volume transfer over 100 cycles. As indicated in Fig. 6 (a), the electrolyte volumes can periodically be rebalanced from the positive to the negative side. Thus, the capacity of the 5 kW/10 kWh VRFB system can be recovered compared to the results without the electrolyte shunt design, as shown in Fig. 6 (b).

4.5. Efficient and robust pump flow rate control

14

15

16

17

18

19

20

22

25

26

27

28

29

Dynamic control of the electrolyte flow rate is critical to improving the efficiency of VRFB systems [22]. To do so, various studies have been reported in the literature to investigate the optimal flow rates for VRFB systems. Wang et al. [1] summarised several model-based methods for optimisation of flow rates. These methods are proposed to achieve point-based or dynamic optimisation through the operation based on different local minimum searching algorithms. However, these model-based optimisation methods lack robustness which needs a highly accurate

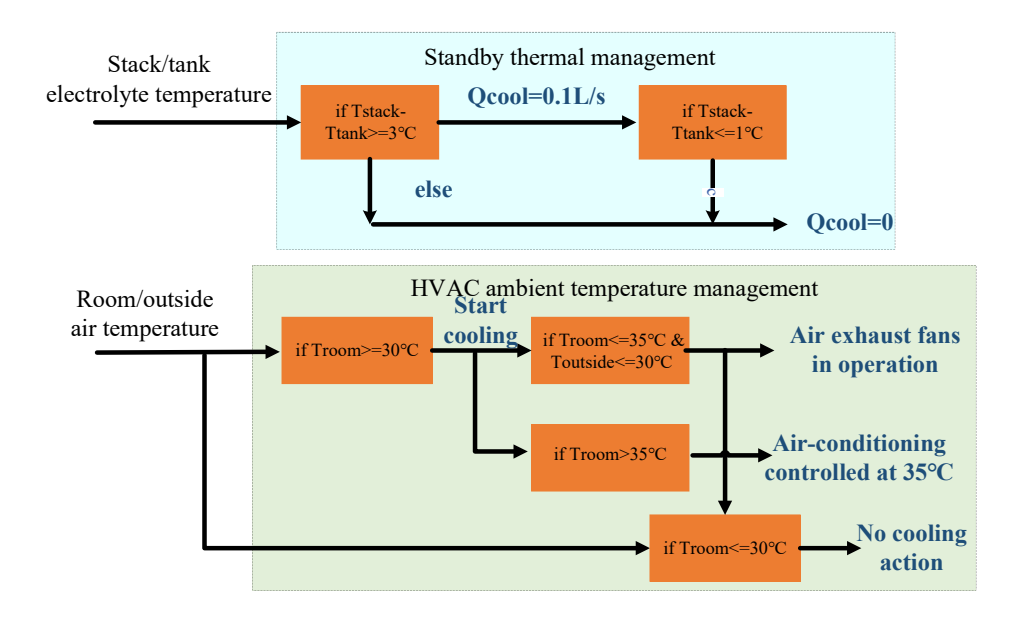


Figure 7: A conceptual thermal management design using cooling flow rate and HVAC air exchange and cooling methods

model to provide the state information in real-time. Most importantly, solving these dynamic optimisation problems is computationally demanding, making this an impractical approach for commercial-scale VRFB-BMS with constrained resources. For example, gradient-based search methods and evolutionary algorithms are used to solve the optimisation problem [43, 44].

To overcome these issues, Wang et al. [22] proposed an approach that involves two stages. In the first stage, which occurs offline, a model-based nonlinear dynamic optimisation (MNDO) is solved to obtain optimal flow rate under different currents when the VRFB system is fully balanced. The proposed MNDO method uses an iterative optimisation framework to find the optimal flow rate at each time step. Once the optimal flow rate values are obtained, in the second stage, certain solutions are chosen to generate a 2D look-up table using the cubic spline interpolation/extrapolation technique. The look-up table is then used in the VRFB BMS for rapid and accurate online flow rate control. A 100 cycles constant charge/discharge test was carried out to validate the effectiveness of the proposed online flow rate control method with electrolyte imbalance in the VRFB system. The results proved that the proposed look-up table method achieves almost the same performance in reducing the overall losses of the VRFB system compared to the MNDO method. Moreover, the proposed approach is more computationally efficient compared to other dynamic flow rate optimisation methods without the need to have an accurate state estimation of the VRFB system. In this study, we use the identical stack design as described in [22], allowing the use of the optimal 2D look-up table in this paper. Both pumps are designed to maintain a steady flow rate of 0.4 L/s for 1 minute following the conclusion of the standby period, preparing the VRFB system for charge and discharge activities. This is to provide a moderate initial electrolyte flow rate to prevent overcharging/discharging issues due to the self-discharge reactions that lead to low electrode surface concentration.

11

12

13

14

15

16

17

18

19

20

21

4.6. Thermal management

Thermal management is important in reducing the thermal precipitation of vanadium ions that causes a non-reversible capacity loss in VRFB systems. Tang et al. [8] revealed the significance of using a cooling flow rate to reduce the thermal imbalance of the electrolyte within the stack and tank due to the high heat generation from the crossover during the standby period. The electrolyte flow rate is critical for absorbing self-discharge heat because of the low heat-exchange capability of the VRFB stack. However, because of the large volume of the electrolyte in the half-system, it is not practical to cool the entire VRFB system via electrolyte circulation alone. Employing an HVAC system to maintain a cooler ambient temperature is the most feasible method for achieving adequate heat dissipation from the VRFB system through passive thermal management. Note that in most literature, the thermal precipitation threshold for the electrolyte is defined as 40° C at high SOC levels [6, 8, 10]. However, from the experimental validation results in [45], V^{5+} tends to precipitate above 35° C. In current VRFB electrolyte designs, different stabilising additives are added during the electrolyte preparation stage to increase the thermal stability of vanadium ions [46]. For commercial-scale VRFB systems, the thermal threshold is normally set to $35-50^{\circ}$ C for ambient operating temperatures [47, 48, 49].

In this study, it is assumed that the maximum ambient temperature is 35°C to prevent the stack electrolyte temperature from reaching 40°C to have thermal precipitation [8, 14]. The thermal management strategy in this BMS design involves integrating multiple VRFB systems within a confined space, modelled after the practical example of the Roseworthy solar farm and battery at the University of Adelaide [50]. An HVAC system is integrated with the BMS to control the room temperature after measuring the room and outside air temperature using sensors. The design of the thermal management system is presented in Fig. 7. The standby thermal management is achieved using a small cooling flow rate of 0.1 L/s. If the stack and tank electrolyte temperature disparity exceeds 3°C, the cooling flow rate will start and stop only when this disparity is reduced to 1°C. The HVAC system will be activated when the room temperature exceeds 30°C. In addition, air exhaust fans are used as soon as the outside air temperature drops below 30°C. Furthermore, when the room temperature exceeds 35°C, the air conditioning system will be used to maintain the room temperature at 35°C. Once the room temperature is lower than 30°C, the exhaust fans and air conditioners will be turned off to save energy.

5. Performance of the proposed BMS

In this section, the performance evaluation of the proposed BMS design is reported based on the optimal BESS power scheduling profile using real PV/load/temperature data of several unique residential profiles from Australian Capital Territory (ACT) using the NextGen dataset [37]. The time of use (ToU) tariff and the solar feed-in tariff (FiT) are obtained from Origin Energy for the same location [51].

5.1. Case 1: A 15-day study without thermal management issues

In Case 1, the 5 kW/10 kWh VRFB system is used in residential applications to reduce the electricity costs for residents. In this study, the load demand and PV generation profiles of a single user in the ACT, Australia, during summer are considered [37]. Fig. 8 (a) illustrates the deployment of the VRFB system in a residential setting with an EMS. The consumer is connected to the grid and can purchase electricity from a retailer when needed. The EMS is assumed to have access to a perfect forecast of load demand and PV generation to determine the optimal charge

and discharge power of the VRFB system for one day ahead. The objective is to minimise the electricity cost of the consumer. The EMS design in this paper is identical to the work by Wang et al. in [52], which used a linear state of energy (SOE) model for remaining energy estimation, similar to the majority of battery energy management studies. Moreover, the EMS applied in this study bears similarity to some commercial residential EMS or smart solar inverter architectures, while necessitating minimal computational resources. The battery power of 1 kW-5 kW for charging and 0.2-5 kW for discharging, the rated energy capacity of 10 kWh and the round-trip efficiency of 70% are assumed for the VRFB system. The optimisation problem solved by the EMS is given below [52]:

$$\min \sum_{t \in \mathcal{H}} \left(C_t^{im} P_t^{im} \right) \Delta t - \left(C_t^{ex} P_t^{ex} \right) \Delta t \tag{42a}$$

s.t.
$$SOE_t = SOE_{t-1} + \eta_{rt} \frac{P_t^{ch} u_t^{ch} \Delta t}{E_n} - \frac{(P_t^{dis} - P^{aux}) u_t^{dch} \Delta t}{E_n} \quad \forall t \in \mathcal{H},$$
 (42b)

$$SOE_0 = 10\%, (42c)$$

$$SOE_{t_f} = SOE_0, (42d)$$

$$0 \le SOE_t \le 1 \quad \forall t \in \mathcal{H},\tag{42e}$$

$$0 \le u_t^{ch} + u_t^{dch} \le 1 \quad \forall t \in \mathcal{H}, \tag{42f}$$

$$P_{min}^{ch} + P^{aux} \le P_t^{ch} \le \min\left(\alpha_{ch} + \beta_{ch} P_{max}^{ch}, P_{max}^{dch}\right) + P^{aux} \quad \forall t \in \mathcal{H},$$

$$P_{min}^{dch} + P^{aux} \le P_t^{dch} \le \min\left(\alpha_{dch} + \beta_{dch} P_{max}^{dch}, P_{max}^{dch}\right) + P^{aux} \quad \forall t \in \mathcal{H},$$

$$(42g)$$

$$P_{min}^{dch} + P^{aux} \le P_t^{dch} \le \min\left(\alpha_{dch} + \beta_{dch} P_{max}^{dch}, P_{max}^{dch}\right) + P^{aux} \quad \forall t \in \mathcal{H}, \tag{42h}$$

$$P_{t}^{pv} + (P_{t}^{dis} - P^{aux})u_{t}^{dch}\eta_{inv} - P_{t}^{ch}u_{t}^{ch}/\eta_{inv} = P_{t}^{ex} - P_{t}^{im} + P_{t}^{load}, \quad \forall t \in \mathcal{H}$$
 (42i)

The definitions, values, and types of symbols in the EMS optimisation formulation are presented in Table 4 in Appendix A. The ToU tariff and solar FiT profiles, as well as sample load, PV, and temperature profiles, are shown in Fig. 8 (a) for an anonymous user. The optimal BESS power dispatch profile is obtained by solving this optimisation problem in MATLAB using the Gurobi solver [53] on a desktop with Intel^(R) Core^(TM) i7-10700 CPU @ 2.90 GHz and 16 GB RAM. Using 5 days of distinct load demand and PV generation data, the battery operation is simulated over a total of 15 days by repeating these profiles three times. This is because the original data exhibits data loss during certain complete days. Another factor contributing to this issue is that many users have minimal electricity consumption at night, rendering the battery system operation unnecessary. This situation is not ideal for demonstrating the results of BMS design. The electrolyte concentration of the VRFB system is assumed to be completely balanced. A minor imbalance in electrolyte volume (244 L in the positive tank and 236 L in the negative tank) is introduced to assess the auto-rebalancing mechanism within the BMS using a hydraulic shunt. The simulation results for battery operation are shown in Fig. 9 (a) for 15 days. The optimal values are then sent to the BMS for action, where a detailed dynamic model of VRFB is used to calculate SOC and temperature profiles. These profiles are shown in Figs. 9 (b) and (c). The results presented in Fig. 9 (c) reveal that the VRFB system rarely encounters thermal management issues. This is attributed to its effective heat exchange capability and the low heat production rate resulting from its large scale. In practical scenarios, thermal management for industrial or commercial-scale VRFB systems is generally unnecessary if the systems are not operated under intensive conditions and the ambient temperature remains below 35°C.

10

11

13

14

15

16

17

18

20

21

22

23

24

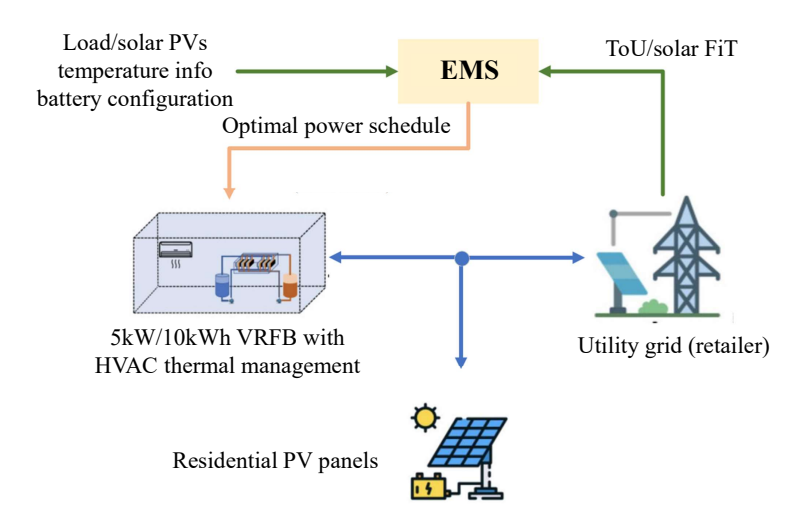
25

26

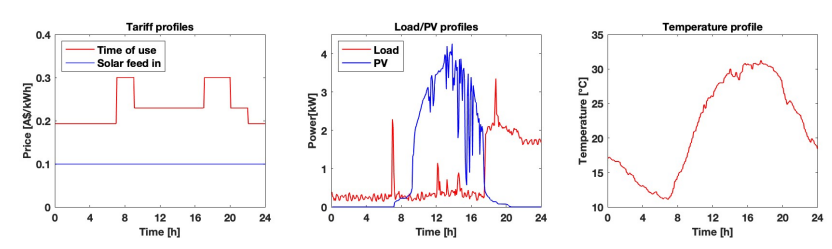
27

28

29



(a) The schematic of a VRFB BMS-EMS system in residential application



(b) Sample tariffs, load, PV, and temperature profiles for a random user

Figure 8: VRFB BMS-EMS system used in Case 1 with a sample load, PV, and temperature profiles, as well as ToU and solar FiT.

More simulation results are presented in Fig. 10 to further demonstrate the efficacy of the proposed VRFB-BMS design. Firstly, the results of automatic electrolyte rebalancing using a hydraulic shunt, shown in Fig. 10 (a), indicate that electrolyte volume rebalancing is achieved on day 9 using hydraulic shunt valve control. Secondly, the results depicted in Fig. 10 (b) reveal that the use of a simple half-cell potential method with reference cells leads to highly precise half-system SOC estimation over a 15-day simulation period. Additional results are shown in Fig. 10 (c) over the same 15-day period, assuming the VRFB system had an electrolyte imbalance issue prior to operation, as mentioned in Section 4.3. The results show that the proposed method continues to deliver exceptional performance even when the VRFB system exhibits significant imbalance issues. Most importantly, the proposed computationally efficient and robust flow rate control method achieves a significant round-trip efficiency improvement to 64.4% from 56.3% obtained with a constant flow rate of 0.4 L/s.

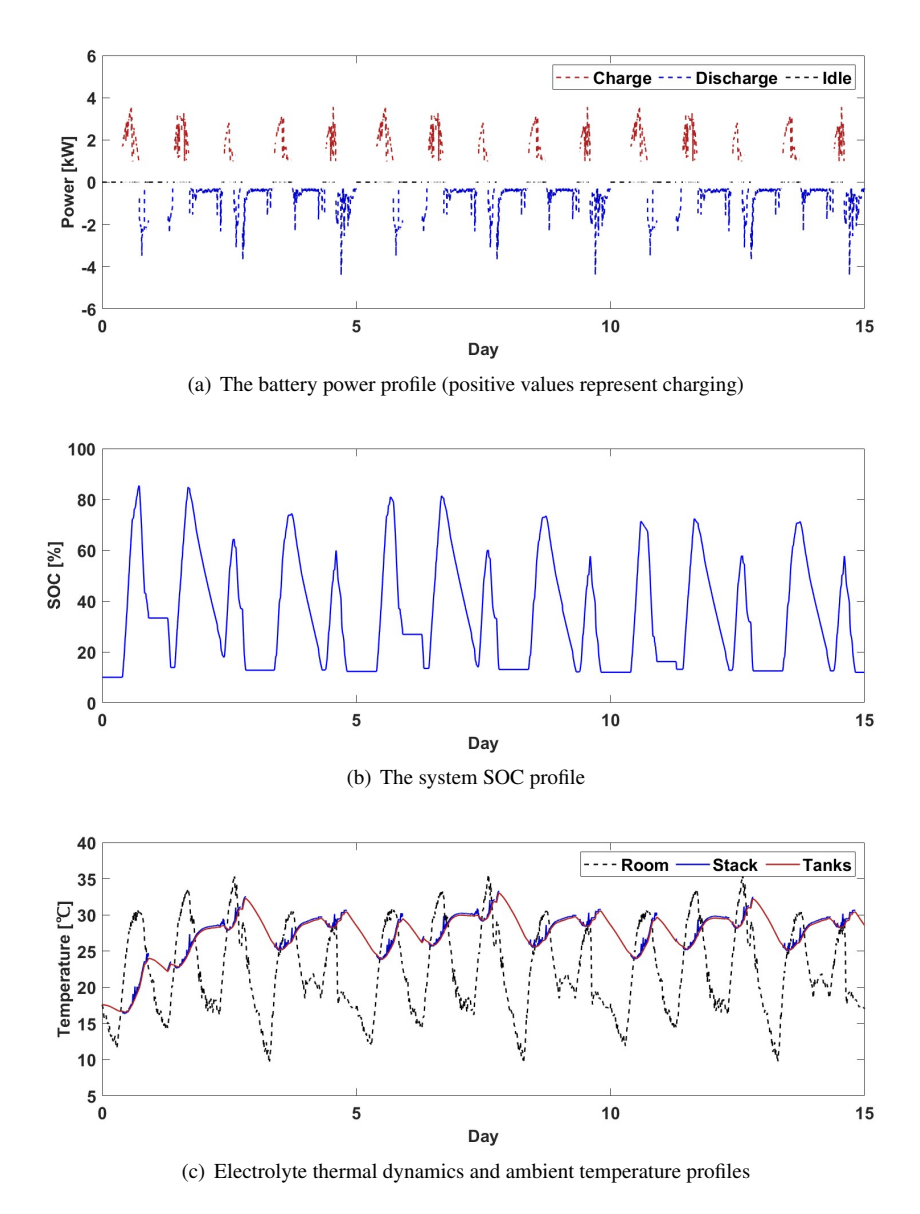
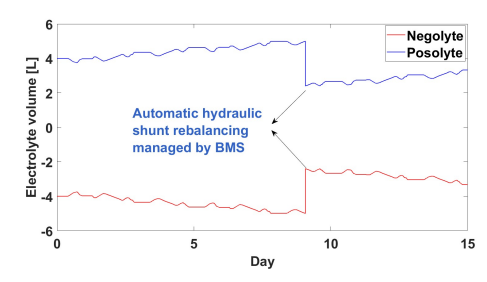


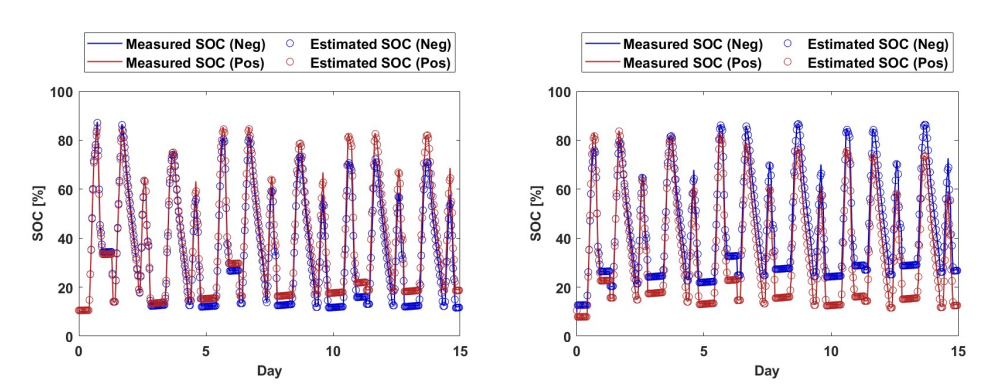
Figure 9: The power profile, system SOC and temperature profiles of the 5 kW/10 kWh VRFB system over 15 days

5.2. Case 2: A 15-day test using real residential profiles with thermal management issues

In the simulation study presented in Section 5.1, there are no problems related to thermal management because the ambient temperature remains within acceptable limits. However, when the VRFB system is placed in an environment with limited heat exchange capacity and added heat produced by the pump and inverter, the room temperature is likely to exceed the acceptable limits. This could be exacerbated by hot summer days in many places and areas close to the equatorial with high solar radiation rates, where the inside temperature can easily exceed 35°C.



(a) Electrolyte volume variations over the half-systems (assume a 8 L electrolyte volume imbalance occurred in day 1)



(b) Half-system SOC profiles assumed the system concentration is fully balanced contraction is fully balanced some tration is not balanced as the case in Section 4.3

Figure 10: The electrolyte volume and half-system SOC profiles over 15 days of simulation

As a result, active cooling using an HVAC system is necessary to guarantee effective thermal management. This section presents the results of a simulation aimed at validating the proposed thermal management approach using an HVAC system. It assumes that the outside air temperature oscillates between 25°C and 40°C in a sinusoidal pattern, as described in [10], to model the uninterrupted operation of a single VRFB system over a span of 15 days, as detailed below:

$$T_{\text{air}} = (T_{\text{max}} - T_{\text{min}}) \cdot \sin^2(\omega t + \varphi) + T_{\text{min}}$$
(43)

where $T_{\rm min}$ and $T_{\rm max}$ are the minimum/maximum ambient air temperature within a day. ω and φ are the angular frequency and phase in rad/s and rad, respectively. Moreover, the 5 kW/10 kWh VRFB system will continue to operate in standby mode when there is no power applied to simulate the rapid rise in stack electrolyte temperature. In this case, the 5 kW/10 kWh VRFB system is installed in a small room with a dimension of 5 m × 4 m × 3 m. In addition, it is assumed that 5% of the inverter's power losses and 20% of the hydraulic pump's power losses from their electric circuits contribute to heat generation. The air mass flow through the air exhaust fan is 0.90 kg s⁻¹, and the exhaust fan power consumption is 140 W. The formulation of the room temperature model and the power consumption of the air-conditioning system is extended based

10

13

on the model from [10]:

$$\frac{d\dot{Q}_{cool}}{dt} = (T_{room} - T_{out}) \cdot M_{fan} \cdot C_{air} + \frac{d\dot{Q}_{ac}}{dt}$$
(44)

$$\frac{d\dot{Q}_{loss}}{dt} = (T_{out} - T_{room}) \cdot h \cdot A_{wall} \tag{45}$$

$$\frac{dT_{room}}{dt} = \frac{1}{M_{air} \cdot C_{air}} \cdot \left(\frac{d\dot{Q}_{loss}}{dt} + \frac{d\dot{Q}_{heat}}{dt} - \frac{d\dot{Q}_{cool}}{dt} \right)$$
(46)

$$\frac{d\dot{Q}_{heat}}{dt} = \left(T_n + T_p - 2 \cdot T_{room}\right) \cdot U_t \cdot A_t + \alpha_{pump} \cdot P_{pump} + \alpha_{inv} \cdot P_{VRFB} \tag{47}$$

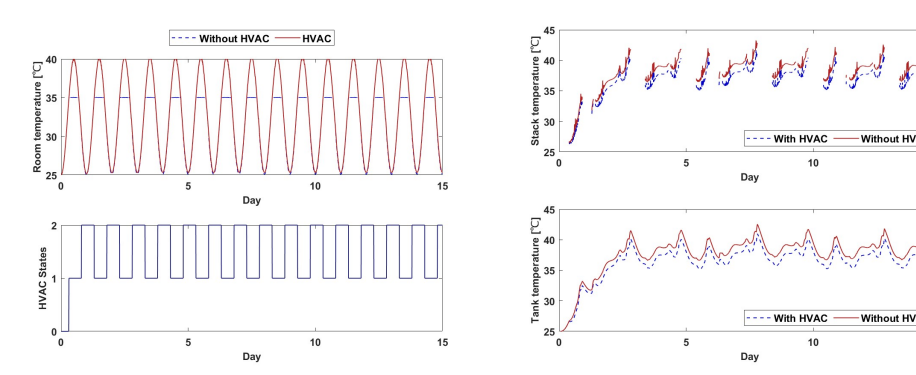
$$P_{ac} = \frac{d\dot{Q}_{ac}}{dt} / EER \tag{48}$$

Table 3: Parameters specifications of the room thermal model

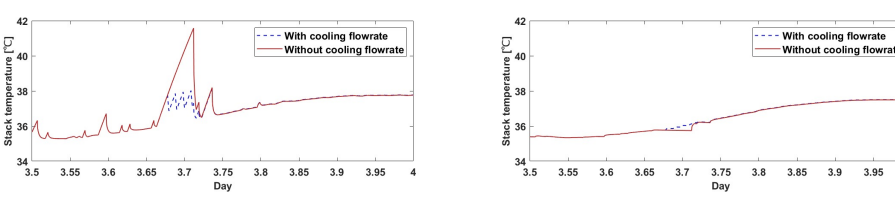
Symbol	Definition	Value
A_{wall}	Total surface of walls in m ²	94
h	Heat transfer coefficient of concrete in W m ⁻² K ⁻¹	5.32
M_{fan}	Air mass flow through fan in kg s ⁻¹	0.90
C_{air}	Heat capacity of air in J kg ⁻¹ K ⁻¹	1020
α_{pump}	Heat loss percentage during pump operation in %	20
α_{inv}	Heat loss percentage during inverter operation in %	5
M_{air}	Air mass inside the room in kg	77
EER	Energy efficiency ratio	3

Note the parameters specifications of the room thermal model are given in Table 3. Figs. 11 (a) and (b) illustrate the simulation results for 15 days with and without the proposed thermal management scheme using an HVAC. In particular, Fig. 11 (a) clearly shows that employing HVAC keeps the maximum room temperature at 35°C, meeting the thermal management goal. The design of the individual operation using air exhaust fans is to ensure that the outside air temperature is adequate to provide heat exchange through the ventilation operation as the results given in Fig. 11 (a). For example, the air exhaust fan operates when the outside air temperature is below 30°C, and the air-conditioning is designed to regulate the temperature inside the battery room once the internal air temperature exceeds 35°C in the absence of enough cooling capacity. Further results in Fig. 11 (b) indicate that room temperature control is effective in decreasing the electrolyte temperature in the stack and tank to prevent the electrolyte temperature from being exposed above the thermal precipitation limit (40°C) for a long period of up to 3 hours. The power usage for a 15-day period is approximately 103.5 kWh, demonstrating the efficiency of the thermal management design in conserving energy.

More results are shown in Figs. 11 (c) and (d) to demonstrate the effectiveness of using a cooling flow rate in reducing the accumulated crossover heat inside the stack. In Fig. 11 (c), rapid reductions in stack electrolyte temperature to prevent overheating that could cause thermal precipitation can be observed on the third day during the standby period to prevent overheating that can cause thermal precipitation. However, the cooling flow rate cannot improve the overall heat exchange capacity of the entire VRFB system. The results presented in Fig. 11 (d) reveal that there is negligible variation in the tank electrolyte temperature, underscoring the critical role



(a) The room temperature and HVAC status profiles over (b) The stack and tank electrolyte temperature profiles 15 days with and without HVAC operation for thermal over 15 days with and without HVAC operation for thermanagement (HVAC status: 1 stands for air-conditioning mal management operation and 2 stands for ventilation operation by using air exhaust fans



(c) The stack electrolyte temperature profiles in a day with (d) The tank electrolyte temperature profiles in a day with and without cooling flowrate and without cooling flowrate

Figure 11: Temperature and HVAC system operational profiles for a single 5 kW/10 kWh VRFB system inside a small room

of HVAC operation in the regulation of room air temperature.

2 6. Conclusion

12

13

In this paper, an advanced VRFB-BMS scheme is designed and validated using a newly proposed zero-dimensional model that incorporates all vanadium ion crossover and electrolyte transfer mechanisms. Additionally, a genuine 5 kW VRFB stack design is employed in the model development, and several case studies are provided next. Detailed explanations are subsequently provided to illustrate the BMS scheme design in terms of operational mode control, hydraulic regulation, SOC estimation, and thermal management. In this study, real residential user profiles are used to validate the design of the VRFB-BMS to accurately estimate SOC, and to perform operational mode control, capacity recovery, auxiliary energy savings, and thermal management. The key findings of this paper are:

• An efficient and practical VRFB-BMS has been developed that can be integrated with an EMS to meet economic and various other objectives for users.

- A highly accurate SOC estimation method is proposed and comprehensively evaluated in comparison with other mainstream methods. Effective and efficient hydraulic control methods are proposed to achieve energy saving and capacity recovery.
- This study suggests that an effective design would include a hybrid thermal management system that combines electrolyte circulation with an HVAC system to effectively manage thermal conditions and reduce capacity loss.
- Long-term operational simulations over 15 days are conducted for further validations. Energy savings and thermal management performance are reported using the proposed advanced VRFB-BMS design.

For future work, an in-depth analysis of the precipitation level of different vanadium species is crucial to designing a more sophisticated thermal management system that can help reduce HVAC energy consumption considering different designs of the VRFB system and its long-term impact. Additional evaluation of hydraulic flow rate control is necessary to avoid overpressure on the membrane that could cause damage. Furthermore, the selection of sensor configurations in the advanced VRFB-BMS design requires in-depth cost-benefit analysis to balance the accuracy and cost requirements in industrial and commercial applications. Above all, it would be valuable to implement this advanced VRFB-BMS scheme design on the hardware for better assessment and model refinement.

19 Acknowledgment

2

3

This project is supported by the Australian Government Research Training Program (RTP) through the University of Adelaide, and a supplementary scholarship is provided by the Microgrid Battery Deployment project, which is funded by the Future Battery Industries Cooperative Research Centre (FBICRC) as part of the Commonwealth Cooperative Research Centre Program, Australia.

25 Declaration of Generative AI and AI-assisted technologies in the writing process

During the preparation of this work, the authors used Writefull/Grammarly for grammar checking. After using these tools, the authors reviewed and edited the content as needed and take full responsibility for the content of the publication.

29 CRediT authorship contribution statement

Hao Wang: Conceptualization, Investigation, Methodology, Software, Validation, Formal analysis, Writing – original draft, Writing – review & editing, Visualization. S. Ali Pourmousavi: Conceptualization, Writing – review & editing, Supervision, Project administration. Wen L. Soong: Conceptualization, Methodology, Writing – review & editing, Supervision. Xinan Zhang: Writing – review & editing, Methodology, Supervision. Aleksandar N. Nikoloski: Writing – review & editing, Methodology. Nesimi Ertugrul: Writing – review & editing.

Appendix A:

Table 4: The definition of symbols, their value and type in the HEMS formulation for optimal energy dispatch of the 5 kW/10 kWh VRFB system [52] (The DV in the table stands for decision variable and the coefficients for battery charging/discharging power regulation are designed to fully charge or discharge the VRFB system)

Symbol	Definition	Type
C_t^{im}	Cost of imported electricity at timestep <i>t</i> (Time of use tariff in A\$/kWh)	Variable
C_t^{ex}	Revenue of exported electricity to the grid at timestep t (Solar feed-in tariff in A\$/kWh)	Variable
P_t^{im}	Residential imported power from the grid at timestep <i>t</i> in kW	Real number DV
P_t^{ex}	Residential exported power to the grid at timestep <i>t</i> in kW	Real number DV
SOE_t	Estimated remaining energy in the battery at timestep t in $\%$	Variable
u_t^{ch}	Battery status indicator during charging at timestep <i>t</i> (1: in charging, 0: idle)	Binary DV
$\begin{array}{c} P_t^{im} \\ P_t^{ex} \\ \hline \\ SOE_t \\ u_c^{ch} \\ u_t^{ch} \\ \hline \\ P_t^{ch} \\ \hline \\ P_t^{dch} \\ \hline \\ P_t^{in} \\ P_t^{in} \\ \hline \\ P_$	Battery status indicator during discharging at timestep <i>t</i> (1: in discharging, 0: idle)	Binary DV
P_t^{ch}	Battery charge power at timestep <i>t</i> in kW	Real number DV
P_t^{dch}	Battery discharge power at timestep <i>t</i> in kW	Real number DV
P_t^{pv}	PV power generation at timestep t in kW	Variable
P_t^{load}	Load power at timestep t in kW	Variable
P_{min}^{ch}	Minimum charge power (1 kW)	Constant
P_{min}^{dch}	Minimum discharge power (0.2 kW)	Constant
P_{max}^{ch}	Maximum charge power (5 kW)	Constant
P_{dch}^{max}	Maximum discharge power (5 kW)	Constant
Paux	Auxiliary power of the VRFB (0.1 kW)	Constant
α^{ch}	Coefficient in Eq. (42g) for battery charging power regulation (10 kW)	Constant
β^{ch}	Coefficient in Eq. (42g) for battery charging power regulation (-9 kW)	Constant
α^{dch}	Coefficient in Eq. (42h) for battery discharging power regulation (1 kW)	Constant
β^{dch}	Coefficient in Eq. (42h) for battery discharging power regulation (6 kW)	Constant
E_n	Nominal (rated) energy capacity of the VRFB system (10 kWh)	Constant
SOE_{min}	Minimum SOE level during the operation (0)	Constant
SOE_{max}	Maximum SOE level during the operation (100%)	Constant
η_{inv}	DC-AC Inverter/AC-DC battery charger efficiency (95%)	Constant
η_{rt}	Round-trip efficiency of the 5 kW/10 kWh VRFB system (70%)	Constant

References

- [1] Hao Wang, S Ali Pourmousavi, Wen L Soong, Xinan Zhang, and Nesimi Ertugrul. Battery and energy management system for vanadium redox flow battery: A critical review and recommendations. *Journal of Energy Storage*, 58:106384, 2023.
- [2] Mohammad Waseem, Mumtaz Ahmad, Aasiya Parveen, and Mohd Suhaib. Battery technologies and functionality
 of battery management system for evs: Current status, key challenges, and future prospectives. *Journal of Power Sources*, 580:233349, 2023.
- 8 [3] Andrea Trovò. Battery management system for industrial-scale vanadium redox flow batteries: Features and operation. *Journal of Power Sources*, 465:228229, 2020.
- [4] Massimo Guarnieri, Andrea Trovò, Angelo D'Anzi, and Piergiorgio Alotto. Developing vanadium redox flow
 technology on a 9-kw 26-kwh industrial scale test facility: Design review and early experiments. *Applied Energy*,
 230:1425–1434, 2018.
- [5] K Vishnu, Phani Teja Bankupalli, Sumit Pramanick, and Anil Verma. Advanced battery management system for
 standalone vrfb applications. In 2023 11th International Conference on Power Electronics and ECCE Asia (ICPE 2023-ECCE Asia), pages 1805–1810. IEEE, 2023.
- 16 [6] Andrea Trovò and Massimo Guarnieri. Standby thermal management system for a kw-class vanadium redox flow battery. Energy Conversion and Management, 226:113510, 2020.
- 18 [7] sumitomo. Redox flow battery smart energy innovator sumitomo electric.
- [8] Ao Tang, Jie Bao, and Maria Skyllas-Kazacos. Thermal modelling of battery configuration and self-discharge reactions in vanadium redox flow battery. *Journal of Power Sources*, 216:489–501, 2012.
- [9] Emil Holm Kirk, Filippo Fenini, Sara Noriega Oreiro, and Anders Bentien. Temperature-induced precipitation of v_2o_5 in vanadium flow batteries—revisited. *Batteries*, 7(4):87, 2021.
- [10] Hao Wang, Wen L Soong, S Ali Pourmousavi, Xinan Zhang, Nesimi Ertugrul, and Bingyu Xiong. Thermal dynamics assessment of vanadium redox flow batteries and thermal management by active temperature control. *Journal of Power Sources*, 570:233027, 2023.
- 26 [11] Bing Shu, Maria Skyllas-Kazacos, Jie Bao, and Ke Meng. Hybrid cooling-based thermal management of containerised vanadium flow battery systems in photovoltaic applications. *Processes*, 11(5):1431, 2023.
- [12] Hao Wang, S Ali Pourmousavi, Yifeng Li, Wen L Soong, Xinan Zhang, and Bingyu Xiong. A new zero-dimensional dynamic model to study the capacity loss mechanism of vanadium redox flow batteries. *Journal of Power Sources*, 603:234428, 2024.
- [13] Yifeng Li, Longgang Sun, Liuyue Cao, Jie Bao, and Maria Skyllas-Kazacos. Dynamic model based membrane
 permeability estimation for online soc imbalances monitoring of vanadium redox flow batteries. *Journal of Energy* Storage, 39:102688, 2021.
- 34 [14] Ankur Bhattacharjee and Hiranmay Saha. Development of an efficient thermal management system for vanadium redox flow battery under different charge-discharge conditions. *Applied Energy*, 230:1182–1192, 2018.
- 36 [15] Bahman Khaki and Pritam Das. Voltage loss and capacity fade reduction in vanadium redox battery by electrolyte flow control. *Electrochimica Acta*, 405:139842, 2022.
- Ifel Yuxi Song, Xiangrong Li, Jing Xiong, Linlin Yang, Guoliang Pan, Chuanwei Yan, and Ao Tang. Electrolyte
 transfer mechanism and optimization strategy for vanadium flow batteries adopting a nafion membrane. *Journal of Power Sources*, 449:227503, 2020.
- [17] Ertan Agar, A Benjamin, CR Dennison, D Chen, MA Hickner, and EC Kumbur. Reducing capacity fade in vana-dium redox flow batteries by altering charging and discharging currents. *Journal of Power Sources*, 246:767–774,
 2014.
- [18] Seong Beom Lee, Kishalay Mitra, Harry D Pratt III, Travis M Anderson, Venkatasailanathan Ramadesigan, Babu R
 Chalamala, and Venkat R Subramanian. Open data, models, and codes for vanadium redox batch cell systems: a
 systems approach using zero-dimensional models. *Journal of Electrochemical Energy Conversion and Storage*,
 17(1):011008, 2020.
- [19] Yasser Ashraf Gandomi, DS Aaron, TA Zawodzinski, and MM Mench. In situ potential distribution measurement
 and validated model for all-vanadium redox flow battery. *Journal of The Electrochemical Society*, 163(1):A5188,
 2015.
- 51 [20] Andrea Trovo, Alberto Saccardo, Monica Giomo, and Massimo Guarnieri. Thermal modeling of industrial-scale vanadium redox flow batteries in high-current operations. *Journal of Power Sources*, 424:204–214, 2019.
- [21] Yifeng Li. Advanced Modelling, Optimisation and Control of Vanadium Redox Flow Battery. PhD thesis, The
 University of New South Wales, 2018.
- [55] [22] Hao Wang, S Ali Pourmousavi, Wen L Soong, Xinan Zhang, Nesimi Ertugrul, and Bingyu Xiong. Model-based
 [56] nonlinear dynamic optimisation for the optimal flow rate of vanadium redox flow batteries. *Journal of Energy* [57] Storage, 68:107741, 2023.

- [23] S König, MR Suriyah, and T Leibfried. Innovative model-based flow rate optimization for vanadium redox flow batteries. *Journal of Power Sources*, 333:134–144, 2016.
- [24] Yun Wang and Sung Chan Cho. Analysis and three-dimensional modeling of vanadium flow batteries. *Journal of The Electrochemical Society*, 161(9):A1200, 2014.
- [25] Rajagopalan Badrinarayanan, Jiyun Zhao, KJ Tseng, and Maria Skyllas-Kazacos. Extended dynamic model for ion diffusion in all-vanadium redox flow battery including the effects of temperature and bulk electrolyte transfer.
 Journal of Power Sources, 270:576–586, 2014.
- [26] Kyeongmin Oh, Milad Moazzam, Geonhui Gwak, and Hyunchul Ju. Water crossover phenomena in all-vanadium
 redox flow batteries. *Electrochimica Acta*, 297:101–111, 2019.
- [27] M Pugach, M Kondratenko, S Briola, and A Bischi. Zero dimensional dynamic model of vanadium redox flow battery cell incorporating all modes of vanadium ions crossover. Applied energy, 226:560–569, 2018.
- 12 [28] Chi-Yuan Lee, Chin-Lung Hsieh, Chia-Hung Chen, Yen-Pu Huang, Chong-An Jiang, and Pei-Chi Wu. A flexible 5-in-1 microsensor for internal microscopic diagnosis of vanadium redox flow battery charging process. *Sensors*, 19(5):1030, 2019.
- [29] Andrea Trovò, Giacomo Marini, Walter Zamboni, and Sebastian Dambone Sessa. Redox flow batteries: A glance
 at safety and regulation issues. *Electronics*, 12(8):1844, 2023.
- 17 [30] Sabine Piller, Marion Perrin, and Andreas Jossen. Methods for state-of-charge determination and their applications.

 18 *Journal of Power Sources*, 96(1):113–120, 2001.
- [31] Xiaobo Zhao, Kangsan Kim, and Seunghun Jung. State-of-charge estimation using data fusion for vanadium redox
 flow battery. *Journal of Energy Storage*, 52:104852, 2022.
- 21 [32] Alejandro Clemente, Andreu Cecilia, and Ramon Costa-Castelló. Online state of charge estimation for a vanadium redox flow battery with unequal flow rates. *Journal of Energy Storage*, 60:106503, 2023.
- 23 [33] Ao Tang, Jie Bao, and Maria Skyllas-Kazacos. Dynamic modelling of the effects of ion diffusion and side reactions on the capacity loss for vanadium redox flow battery. *Journal of Power Sources*, 196(24):10737–10747, 2011.
- ²⁵ [34] Sara Corcuera and Maria Skyllas-Kazacos. State-of-charge monitoring and electrolyte rebalancing methods for the vanadium redox flow battery. *Eur. Chem. Bull*, 1(12):511–519, 2012.
- [35] Kittima Ngamsai and Amornchai Arpornwichanop. Analysis and measurement of the electrolyte imbalance in a vanadium redox flow battery. *Journal of Power Sources*, 282:534–543, 2015.
- ²⁹ [36] Yifeng Li. State-of-charge monitoring for vanadium redox flow batteries. *Flow Batteries: From Fundamentals to*³⁰ Applications, 2:627–640, 2023.
- [37] Marnie Shaw, Bjorn Sturmberg, Lin Guo, Xinyu Gao, Elizabeth Ratnam, and Lachlan Blackhall. The nextgen
 energy storage trial in the act, australia. In Proceedings of the Tenth ACM International Conference on Future
 Energy Systems, pages 439–442, 2019.
- [38] Simon Ressel, Florian Bill, Lucas Holtz, Niklas Janshen, Antonio Chica, Thomas Flower, Claudia Weidlich, and
 Thorsten Struckmann. State of charge monitoring of vanadium redox flow batteries using half cell potentials and
 electrolyte density. *Journal of Power Sources*, 378:776–783, 2018.
- Arjun Bhattarai, Nyunt Wai, Rüdiger Schweiss, Adam Whitehead, Günther G Scherer, Purna C Ghimire, Tuti M Lim, and Huey Hoon Hng. Vanadium redox flow battery with slotted porous electrodes and automatic rebalancing demonstrated on a 1 kw system level. *Applied Energy*, 236:437–443, 2019.
- [40] Kara E Rodby, Thomas J Carney, Yasser Ashraf Gandomi, John L Barton, Robert M Darling, and Fikile R Brushett.
 Assessing the levelized cost of vanadium redox flow batteries with capacity fade and rebalancing. *Journal of Power Sources*, 460:227958, 2020.
- [41] Ke Wang, Le Liu, Jingyu Xi, Zenghua Wu, and Xinping Qiu. Reduction of capacity decay in vanadium flow batteries by an electrolyte-reflow method. *Journal of Power Sources*, 338:17–25, 2017.
- [42] Katharina Schafner, Maik Becker, and Thomas Turek. Capacity balancing for vanadium redox flow batteries
 through continuous and dynamic electrolyte overflow. *Journal of Applied Electrochemistry*, 51(8):1217–1228,
 2021.
- 48 [43] Tao Wang, Jiahui Fu, Menglian Zheng, and Zitao Yu. Dynamic control strategy for the electrolyte flow rate of vanadium redox flow batteries. *Applied Energy*, 227:613–623, 2018.
- [44] Yifeng Li, Xinan Zhang, Jie Bao, and Maria Skyllas-Kazacos. Studies on optimal charging conditions for vanadium
 redox flow batteries. *Journal of Energy Storage*, 11:191–199, 2017.
- 52 [45] Shuibo Xiao, Lihong Yu, Lantao Wu, Le Liu, Xinping Qiu, and Jingyu Xi. Broad temperature adaptability of vanadium redox flow battery—part 1: Electrolyte research. *Electrochimica Acta*, 187:525–534, 2016.
- [46] Pavel Loktionov, Dmitry Konev, Roman Pichugov, Mikhail Petrov, and Anatoly Antipov. Calibration-free coulo metric sensors for operando electrolytes imbalance monitoring of vanadium redox flow battery. *Journal of Power Sources*, 553:232242, 2023.
- 57 [47] Rongke Power. Upower datasheet. url=http://www.rongkepower.com/upload/about/upowerchanpinguigeshushineiban3429.pdf.
- 58 [48] E22 Energy Storage Solutions. Vanadium Redox Flow Battery 250kW (1,000kWh)
 59 url=https://www.energystoragesolutions.com/documents/Datasheet-E22-250kW.pdf.

- 1 [49] Largo. A large-scale vertically integrated VRFB system.
- 2 [50] Roseworthy solar farm and energy storage, June 2021. url=https://https://www.adelaide.edu.au/ecoversity/achievements/roseworthy-solar-farm-and-energy-storage.
- [51] Origin Energy. Origin energy, Jan 2024. url=https://www.originenergy.com.au/my/.
- [52] Hao Wang, S Ali Pourmousavi, Wen L Soong, Xinan Zhang, and Rui Yuan. Accurate battery models matter:
 Improving battery performance assessment using a novel energy management architecture. *Journal of Power Sources*, 631:236216, 2025.
- [53] Gurobi. Gurobi optimiser, Jan 2024. url=https://www.gurobi.com/solutions/gurobi-optimizer/.